Cooperative Standoff Target Tracking using Multiple Fixed-wing UAVs with Input Constraints in Unknown Wind

Zhong Liu *, Lingshuang Xiang , Zemin Zhu

Posted Date: 20 July 2023

doi: 10.20944/preprints202307.1347.v1

Keywords: multiple UAVs; cooperative control; target tracking; Lyapunov guidance vector field; unknown background wind

Article

Cooperative Standoff Target Tracking Using Multiple Fixed-Wing UAVs with Input Constraints in Unknown Wind

Zhong Liu [1,*], Lingshuang Xiang [2] and Zemin Zhu [1]

[1] School of Computer Science, Huanggang Normal University, Huanggang 438000, Hubei, China
[2] Changjiang Industry Investment Group CO., LTD, Wuhan 430062, Hubei, China
* Correspondence: 15829732829@163.com; Tel.: +86-158-2973-2829

Abstract: This paper investigates the problem of cooperative standoff tracking using multiple fixed-wing unmanned aerial vehicles (UAVs) with control input constraints. In order to achieve accurate target tracking in the presence of unknown background wind and target motion, a coordinated standoff target tracking algorithm is proposed. The objective of the research is to steer multiple UAVs to fly a circular orbit around a moving target with prescribed intervehicle angular spacing. To achieve this goal, two control laws are proposed, including relative range regulation and space phase separation. On one hand, a heading rate control law based on Lyapunov guidance vector field is proposed. The convergence analysis show that the UAVs can asymptotically converge to a desired circular orbit around the target, regardless of their initial position and heading. Through rigorous theoretical proof, it is concluded that the command signal of the proposed heading rate controller will not violate the boundary constraint on heading rate. On the other hand, a temporal phase is introduced to represent the phase separation and avoid discontinuity of the wrapped space phase angle. On this basis, a speed controller is developed to achieve equal phase separation. The proposed airspeed controller met the requirement of airspeed constraint. In addition, to improve the robustness of the aircraft during target tracking, an estimator is developed to estimate the composition velocity of the unknown wind and target motion. The proposed estimator uses the offset vector between the UAV's actual flight path and the desired orbit which is defined by Lyapunov guidance vector field to estimate the composition velocity. The stability of the estimator is proved. Simulations are conducted under different scenarios to demonstrate the effectiveness of the proposed cooperative standoff target tracking algorithm. The simulation results of indicate that, the temporal-phase-based speed controller can achieve fast convergence speed and small phase separation error. Additionally, the composition velocity estimator exhibits fast response speed and high estimation accuracy.

Keywords: multiple UAVs; cooperative control; target tracking; Lyapunov guidance vector field; unknown background wind

1. Introduction

Tracking a moving ground target is one of the important capabilities of UAVs [1]. Making the tracking process automatic and free of human intervention is essential for reliving the burden on UAV operators and improving the efficiency and safety of UAV missions. The goal of this paper is to develop a control scheme that allows multiple fixed-wing UAVs to cooperatively track a moving ground target in unknown windy conditions.

Target tracking using multiple fixed-wing UAVs remains a challenge. On one hand, the motion of fixed-wing UAVs is subject to various input constrains. To prevent stalling, a fixed-wing aircraft cannot hover and must maintain a positive forward airspeed. Accordingly, the UAVs must fly in a circle around the ground moving target [2]. On the other hand, to avoid collisions and to ensure that the sensors can cover the target, the UAVs need to be evenly distributed around the target and

maintain a certain phase interval [3]. The standoff tracking is a possible solution for target tracking using a team of fixed-wing UAVs. In this pattern, the UAVs keep a certain distance (called standoff radius) from the target and moves in a circular motion (termed standoff circle) at a proper altitude relative to the target.

In cooperative target tracking missions with unknown wind, three main technical issues should be considered: (1) Relative distance regulation, which focuses on how to enable the UAVs to converge to a circular orbit with prescribed standoff radius around the target by controlling their headings [4]. (2) Intervehicle phase separation, which focuses on the distributing the loitering UAVs uniformly over a standoff circle with certain angular phase difference by controlling their airspeeds [5]. (3) Background wind resistance, which focuses on how to achieve robust stability for UAVs performing standoff tracking in the presence of wind and target motion [6].

Relative distance regulation, which aims to steer the UAV to a circular orbit around the target, is the key to achieve standoff tracking of a moving target by a single UAV. Typically, a guidance law is proposed to regulate the position of the UAV on a predefined circular path. The path usually guides the UAV to circle around a ground moving target at a constant distance. Consequently, the UAV trajectory can be expressed as a circle with predefined standoff radius in the target's frame. There are various types of the guidance law, including reference point guidance (RPG) [7–9], Lyapunov guidance vector field (LGVF) [10–14] and so on. Based on a predefined target tracking path, the standoff tracking problem of a ground moving target can be converted into a path following problem [7]. For example, in [8] and [9], a nonlinear guidance law is proposed to achieve path following for curved path. In this approach, each point on the curved path is designated as a reference point, and a lateral acceleration command is generated to drive the UAV to the reference point. However, due to the ground target moving speed is usually much slower than that of the UAV, the RPG method cannot be directly applied to the standoff target tracking problem. As a new form of potential filed, the LGVF is introduced to guide the UAVs to achieve standoff target tracking. In [10], a LGVF is proposed for loiter maneuver around a stationary target. This approach also enables moving target tracking, but it may lead to slow convergence due to constant curvature in the LGVF. To shorten the convergence time, literature [11] combines the tangent with the LGVF, while literature [12,13] add the circulation parameter c into the original LGVF. The shape of LGVF can be adaptively adjusted by changing the circulation parameter. In this way, a faster convergence to the standoff circle can be achieved due to a higher contraction component. Based on the works of [12,13], an offline optimal parameter searching method is presented for selecting the optimal guidance function to shorten the convergence time in [14]. However, this approach has such heavy computational load that it cannot be extended to real-time application scenarios. Although these above methods have been verified to be feasible for the single UAV standoff tracking problem, they only focus on the optimization of LGVF without considering the input constraints of fixed-wing UAV, such as heading rate limitation. If the curvature of the LGVF is too large, the actual trajectory of UAV cannot converge to a standoff circle due to the saturated rudders. Therefore, it is still necessary to design a control law for regulating the relative distance while satisfying the turning rate limitation.

The performance of target localization algorithm is significantly impacted by the relative sensor-target geometry. Observation configurations, or different sensor-target geometries, produce varying estimation error ellipses of target location algorithm. It is worth considering which observation configuration can yield the best target localization results. By minimizing the Cramer-Rao lower bound (CRLB), which provides a lower bound on estimator performance, the uncertainty in estimation process can be reduced. Therefore, literature [15] utilizes the determinant of CRLB to determine the observation configuration that results in a minimal measure of the uncertainty ellipse. According to the conclusions in [15], if only two UAVs perform standoff tracing mission, the intersection angle subtended at the target (called phase separation angle) by two UAV will be $\left(\frac{\pi}{2}\right)$; if the number of UAVs is $N \geq 3$, the phase separation angle between adjoining UAVs will be $\left(\frac{2\pi}{N}\right)$. An optimal configuration should position UAVs at equal angular intervals around the perimeter of the standoff circle. This requires the phase separation in the coordinated standoff tracking problem. Various phase separation methods have been proposed, including model predictive control (MPC)

 doi:10.20944/preprints202307.1347.v1

[16,17], sliding mode control (SMC) [18,19], conical pendulum motion [20], consensus algorithm [21–24] and so on. In [16,17], a nonlinear MPC framework for coordinated standoff tracking by two UAVs is proposed The optimal control outputs for speed and turning rate are generated by minimizing the sum of weighted cost functions that include standoff-distance regulation error and phase separation error in a receding horizon. However, as the number of the UAVs increases, the computational complexity and iterative time required for searching optimal results also increase. In [18], a loitering algorithm based on sliding mode control is presented to control the virtual leader's position on a standoff circle centered at the ground moving target. However, the SMC method suffers from chattering due to the discontinuity of the signum function in the control law. To eliminate chattering, the signum function is replaced by a saturation function in literature [19]. However, both literature [18,19] ignore the vehicle airspeed constraint. The airspeed of the fixed-wing UAV is restricted within lower and the upper bounds. In order to satisfy the airspeed boundary constraint, literature [20] proposes that the UAV reduces its speed by decreasing the standoff radius when flying on the right-hand side of the target and its airspeed reaches the upper bound. Conversely, the UAV increases the standoff radius to increase its airspeed when its airspeed reaches the lower bound. However, this approach causes the distance between the UAV and the target to oscillate, leading to failure in achieve the control objectives of the cooperative standoff target tracking problem. Different from the integrated controller in [20], the heading control channel and velocity control channel are decoupled in [21–24]. The space phase angle is chosen as the coordination variable of the consensus algorithm, allowing for the design of cooperative airspeed controllers for the UAVs. The phase separation angles among the UAVs can asymptotically convergence to the same one, reflecting equal space separation. However, the airspeed constraint is not taken into account in the space phase separation method. Furthermore, the phase separation angles wrapped in $[-\pi, \pi)$ are discontinuous, and will lead to oscillating airspeed control input. It is not beneficial for reducing the space phase separation error. Therefore, it is critical to design a phase separation controller that provides a smooth signal output and meets the airspeed constraint of UAVs in the coordinated standoff tracking problem.

Most of the research mentioned above assumes an ideal non-wind environment or a known constant background wind. However, in practice, background wind is usually present and it affects the performance of the UAVs, especially when the background wind is unknown. In [25], a robust term is added to the standoff tracking control law to obtain disturbance rejection for wind-gust. However, the response time of the robust controller is too long and unsuitable for highly maneuvering target tracking. To quantitatively describe wind dynamics, a simple conservative model (e.g. sine function as in [26] or linear model as in [27]) or a more sophisticated one (e.g. stochastic as in [28]) can be used. In [28], Dryden model [29] and Davenport model [30] are used to describe the dynamics of wind in high altitude or near the ground, respectively. The unscented Kalman Filter (UKF) is introduced to estimate the velocity of background wind. However, the accuracy of the wind speed estimation largely depends on the accuracy of the constructed wind dynamic model. In reality, wind is stochastic and time-varying, which makes it difficult to be modeled. In literature [31], an adaptive estimator is utilized to estimate the wind velocity. In the case of a stationary target without wind, the vehicle trajectory converges to a circle orbit (called perfect trajectory or orbit) by implementing a designed standoff tracking control law. However, for a moving target with wind, the actual trajectory cannot converge to the perfect one due to the disturbance caused by the wind and target motion. The wind velocity estimation can be obtained by reducing the offset between the actual vehicle trajectory and the perfect trajectory. However, the convergence rate of the estimator is slow because it only uses the radial distance of the offset. Therefore, designing a wind velocity estimator that has high accuracy and fast convergence rate remains challenging.

This paper addressed the challenges of cooperative standoff target tracking using multiple fixed-wing UAVs with input constraints and the considerations of unknown background wind and target motion. The controllers satisfying the input constraints, such as heading rate and airspeed limitation, are designed to guarantee a team of fixed-wing UAVs to perform efficiently during coordinated standoff tracking missions. The major contributions of the paper are as follows: (1) A heading rate

 doi:10.20944/preprints202307.1347.v1

control law based on LGVF is proposed. We prove that this proposed heading rate controller can guarantee that the UAV can asymptotically converge to a standoff circle loitering the target under arbitrary initial conditions of the position and heading. To satisfy the limitation of heading rate, the minimum allowable standoff radius is formulated; (2) In order to avoid the discontinuity of space phase angle, a new term called temporal phase is proposed to represent the phase separation. An airspeed control law is introduced to steer a team of UAVs maintaining an optimal observation configuration, which requires distribution around the standoff circle with equal phase separation. Rigorous proofs for global convergence and satisfying airspeed limitation using the proposed speed controller are provided. (3) The target motion and background wind are regarded as external disturbance. The offset vector caused by external disturbance between the actual trajectory and the perfect/desired orbit is utilized to estimate the composition velocity of background wind and target motion. We prove that the estimation result of the proposed estimator asymptotically converges to the true value of the composition velocity.

The remainder of this paper is structured as follows. Sec. 2 presents problem formulation, including assumptions made in this study, a UAV kinematic model with control input constraints, and control objectives. Sec. 3 discusses the problem of standoff tracking using a single UAV. Based on the LGVF, a lateral controller with heading rate input constraint is proposed to regulate the position of a UAV on a circle around the target under the condition of arbitrary initial position and heading. In Sec. 4, we introduce a term called temporal phase to represent the spatial distribution of the UAVs on the standoff circle, and propose cooperative controllers with airspeed input constraint to achieve desired temporal phase separation. In Sec. 5, an online estimator is developed to adapt the proposed heading rate and airspeed controllers to the case of a moving target in the presence of wind. Simulation and experimental results are demonstrated in Sec. 5, followed by summary and conclusions in Sec. 6.

2. Problem Formulations

Without loss of generality, the following assumptions are made to render the problem simpler and well posed.

Assumption 1. *The UAVs flies at a constant altitude, and the target moves in a two-dimensional plane, ignoring their heights.*

Assumption 2. *The position and velocity of the moving target are assumed to be known or well estimated.*

Assumption 3. *The communication between UAVs is ideal without any restrictions, such as limited communication range, packet loss and delay.*

Assumption 4. *The UAV is equipped with a low-level autopilot that holds constant altitude, follows the command inputs of the speed and heading rate.*

2.1. UAV Model

Under the above assumptions, the inertial frame in a two-dimensional planar is constructed. The x and y axes point east and north, respectively. As shown in Figure 1, the kinematic of the UAV is expressed as follows:

Preprints (www.preprints.org) | NOT PEER-REVIEWED | Posted: 20 July 2023 doi:10.20944/preprints202307.1347.v1

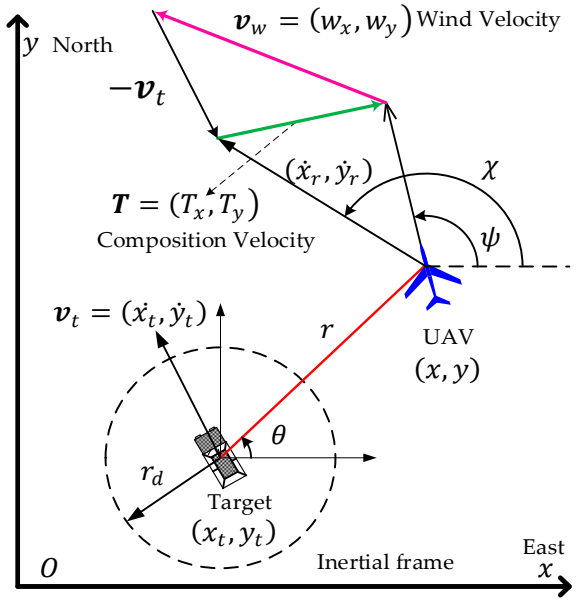

Figure 1. Geometry of ground target tracking in wind.

$$\dot{x} = v_s \cos\psi + w_x; \dot{y} = v_s \sin\psi + w_y; \dot{\psi} = u \tag{1}$$

In Equation (1), $\boldsymbol{v}_w = (w_x, w_y)$ is the background wind velocity. $(x, y) \in \mathbf{R}^2$ is the two-dimensional position of the UAV in the inertial frame. $\psi \in [-\pi, \pi)$ is the UAV heading. v_s is the airspeed of the UAV. u is the heading rate of the UAV. $\boldsymbol{U} = (v_s, u)^{\mathrm{T}}$ is the control input signal followed by the low-level autopilot of the UAV. The airspeed and the heading rate should be enforced on following input constrains.

$$0 < v_{min} \le v_s \le v_{max} \tag{2}$$

$$|u| \le \omega_{max} \tag{3}$$

In Equation (2) and (3), v_{min}, v_{max} are the minimum and maximum airspeed respectively. ω_{max} is the upper bound of heading rate.

The position and velocity of a ground moving target in the inertial frame are denoted as (x_t, y_t) and $\boldsymbol{v}_t = (\dot{x}_t, \dot{y}_t)$, respectively. The distance vector between the UAV and the target is $\boldsymbol{r} = (x_r, y_r)$, and the relative distance is $r = \|\boldsymbol{r}\|$, the observation phase is $\theta \in [-\pi, \pi)$. The relative motion with background wind is expressed as follows

$$\dot{x}_r = v_s \cos\psi + w_x - \dot{x}_t; \dot{y}_r = v_s \sin\psi + w_y - \dot{y}_t; \dot{\psi} = u \tag{4}$$

The target motion and wind are regarded as an external disturbance. These two velocities can be combined to a single velocity term which is called composition velocity, and denoted as $\boldsymbol{T} = (T_x, T_y) = (\dot{x}_t - w_x, \dot{y}_t - w_y)$. Equation (4) can be rewritten as follows:

$$\dot{x}_r = v_r \cos\chi; \dot{y}_r = v_r \sin\chi; \dot{\chi} = \lambda_u(\psi) u \tag{5}$$

In Equation (5), $\chi \in [-\pi, \pi)$ is the relative course angle. v_r is the relative speed. $\lambda_u(\psi)$ is the parameter of relative motion model. They are calculated as follows

$$v_r = \sqrt{v_s^2 + T_x^2 + T_y^2 - 2v_s(T_x \cos\psi + T_y \sin\psi)} \tag{6}$$

$$\chi = \arctan\left(\frac{v_s \sin\psi - T_y}{v_s \cos\psi - T_x}\right) \tag{7}$$

Preprints (www.preprints.org) | NOT PEER-REVIEWED | Posted: 20 July 2023 doi:10.20944/preprints202307.1347.v1

$$\lambda_u(\psi) = \frac{v_s^2 - v_s(T_x cos\psi + T_y sin\psi)}{v_r^2} \geq \frac{1}{2} \tag{8}$$

The relative motion as shown in Equation (5) can be expressed in polar coordinates as

$$\begin{bmatrix} \dot{r} \\ r\dot{\theta} \end{bmatrix}_{\text{UAV}} = \begin{bmatrix} \dot{x}_r cos\theta + \dot{y}_r sin\theta \\ -\dot{x}_r sin\theta + \dot{y}_r cos\theta \end{bmatrix} = \begin{bmatrix} v_r cos(\chi - \theta) \\ v_r sin(\chi - \theta) \end{bmatrix} \tag{9}$$

2.2. The Objectives of Control Problem

As shown in **Error! Reference source not found.**, there is a team of UAVs (A_i, $i = 1,2,\ldots,N$) performing cooperative standoff tracking mission for a ground moving target in unknown background wind. In the process of tracking, on one hand, each UAV needs to circle around the target to maintain a constant relative distance. On the other hand, the loitering UAVs are distributed around the target with equal phase separation to avoid collisions and maximize coverage of sensors. The following three control objectives need to be achieved for the multi-UAVs cooperative standoff tracking control problem.

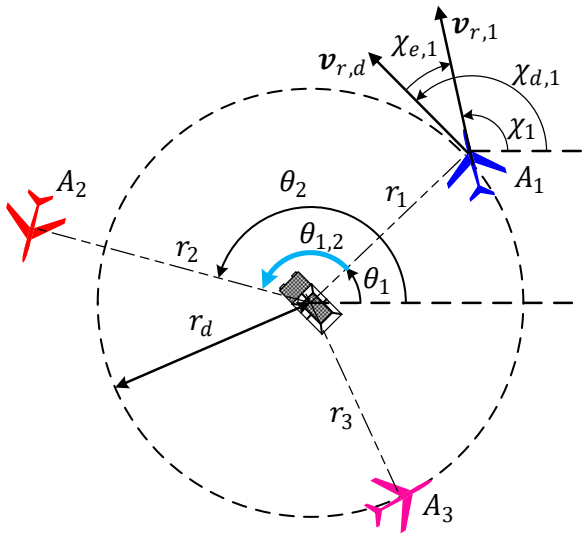

Figure 2. Illustration of cooperative standoff target tracking.

The following three control objectives need to be achieved for the multi-UAVs cooperative standoff tracking control problem.

i) **Control objective 1: Relative distance regulation.** The relative distance r_i between the UAV A_i and the target should be converged to the desired standoff radius r_d.

$$\Delta r_i = r_i - r_d \longrightarrow 0 \tag{10}$$

ii) **Control objective 2: Relative course convergence.** The relative course χ_i of the UAV A_i should be converged to the desired relative course $\chi_{d,i}$ to maintain circular motion around the target.

$$\chi_{e,i} = \chi_i - \chi_{d,i} \longrightarrow 0 \tag{11}$$

iii) **Control objective 3: Intervehicle phase separation.** The phase separation $\theta_{i,j}$ between A_i and its neighbor A_j should be converged to the optimal configuration θ_d.

$$\Delta\theta_i = \theta_{i,j} - \theta_d = \theta_j - \theta_i - \theta_d \longrightarrow 0 \tag{12}$$

According literature [15], the optimal observation configuration θ_d is defined as follows

$$\theta_d = \begin{cases} \pi/2, N = 2 \\ 2\pi/N, N > 2 \end{cases} \tag{13}$$

Preprints (www.preprints.org) | NOT PEER-REVIEWED | Posted: 20 July 2023 doi:10.20944/preprints202307.1347.v1

Therefore, when studying the multi-UAVs cooperative standoff tracking control problem, the following three issues are mainly considered in this paper.

(a) How to design the lateral control law subject to the heading rate constraint (Equation (3)) to regulate the relative course of A_i, so that A_i could fly along the standoff circle with radius r_d around target. It means that the objectives 1 and 2 are both achieved.
(b) How to design the longitudinal control law subject to the airspeed limitation (Equation (2)) to guarantee that the loitering UAVs are distributed over the standoff circle with equal phase separation. It means that the control objectives 3 is achieved.
(c) How to estimate the composition velocity of wind and target, in order to improve the performance of the UAVs during the tracking in presence of wind and target motion.

3. Standoff Tracking Using a Single UAV

3.1. Guidance Law Based on LGVF

In [10], the desired relative course is generated from a LGVF that guides the UAV to circle around the target with a predefined standoff radius r_d. The LGVF for a standoff target tracking can be described as follows

$$\begin{bmatrix}\dot{x}_r\\ \dot{y}_r\end{bmatrix}_{\mathrm{GF}} = -v_s\begin{bmatrix}\left(\frac{x_r}{r}\right)\left(\frac{r^2-r_d^2}{r^2+r_d^2}\right)+\left(\frac{y_r}{r}\right)\left(\frac{2rr_d}{r^2+r_d^2}\right)\\ -\left(\frac{x_r}{r}\right)\left(\frac{2rr_d}{r^2+r_d^2}\right)+\left(\frac{y_r}{r}\right)\left(\frac{r^2-r_d^2}{r^2+r_d^2}\right)\end{bmatrix} \tag{14}$$

Define the following vector field angle $\phi_{\mathrm{GF}} \in [0,\pi)$

$$\cos\phi_{\mathrm{GF}} = \frac{r_d^2-r^2}{r^2+r_d^2}; \sin\phi_{\mathrm{GF}} = \frac{2rr_d}{r^2+r_d^2} \tag{15}$$

Then, Equation (15) can be expressed in polar coordinates as follows

$$\begin{bmatrix}\dot{r}\\ r\dot{\theta}\end{bmatrix}_{\mathrm{GF}} = \begin{bmatrix}cos\theta & sin\theta\\ -sin\theta & cos\theta\end{bmatrix}\begin{bmatrix}\dot{x}_r\\ \dot{y}_r\end{bmatrix}_{\mathrm{GF}} = \begin{bmatrix}v_s cos\phi_{\mathrm{GF}}\\ v_s sin\phi_{\mathrm{GF}}\end{bmatrix} \tag{16}$$

A following guidance law is introduced to guide the UAV to fly along the LGVF in (16)

$$\chi_d = \theta + \phi_{\mathrm{GF}} \tag{17}$$

where the observation phase θ is defined by

$$\theta = \begin{cases}\arctan\left({}^{y_r}/_{x_r}\right), & \text{if } r > 0\\ \chi, & \text{if } r = 0\end{cases} \tag{18}$$

The feasibility of the guidance law (17) is given by **Theorem 1**.

Theorem 1. *If the guidance law (17) is applied to the relative motion model of the UAV as shown in (9), the relative distance between the UAV and the target asymptotically converges to the predefined standoff radius, i.e.,* $r \longrightarrow r_d$ *as* $t \longrightarrow +\infty$.

Remark 1. *The proof of Theorem 1 is seen in [10]. It can be observed from Theorem 1 that, in order to achieve standoff tracking, it is required that the relative course* χ *should be always aligned with the desired relative course* χ_d *generated by the guidance law (17).*

3.2. Heading Rate Controller Design Subject to the Input Constraints

According the conclusion of Theorem 1, if χ always is equal to χ_d, the UAV eventually converge to the standoff circle with the desired radius r_d, and preform the standoff target tracking mission successfully. However, in general, there exists an angle error between χ and χ_d initially and the relative course χ cannot be controllable directly. Thus, we need design a heading rate

Preprints (www.preprints.org) | NOT PEER-REVIEWED | Posted: 20 July 2023 doi:10.20944/preprints202307.1347.v1

controller to guarantee that the relative course χ eventually converge to χ_d. In other words, the proposed heading rate controller indirectly control χ by regulating the UAV heading directly.

The relative course error $\chi_e \in [-\pi, \pi)$ can be defined by

$$\chi_e = \chi - \chi_d \tag{19}$$

Differentiating Equation (17) with respect to t leads to the following equation

$$\dot{\chi}_d = \dot{\theta} + \dot{\phi}_{\mathrm{GF}} \tag{20}$$

According Equation (9), the dynamic of the azimuth θ is obtained as

$$\dot{\theta} = \frac{v_r}{r} sin(\chi - \theta) \tag{21}$$

Differentiating Equation (15) with respect to t

$$\dot{\phi}_{\mathrm{GF}} = \frac{2r_d}{r^2 + r_d^2} v_r cos(\chi - \theta) \tag{22}$$

The desired relative course rate can be obtained by substituting (21) and (22) into (20).

$$\dot{\chi}_d = \frac{v_r}{r}[sin(\chi_e + \phi_{\mathrm{GF}}) + sin\phi_{\mathrm{GF}} cos(\chi_e + \phi_{\mathrm{GF}})] \tag{23}$$

It can be observed from (23), when $r \to 0$, $\dot{\chi}_d \to +\infty$. Thus, in order to facilitate engineering application, let $\dot{\chi}_d = \frac{4v_r}{r_d}$ when $r = 0$. Based on the relative course error χ_e (19) and the desired relative course rate $\dot{\chi}_d$ (23), the heading rate controller is designed as follows:

$$u = \begin{cases} \omega, & \text{if } |\omega| \le \omega_{max} \\ \mathrm{sgn}(\omega)\omega_{max}, & \text{if } |\omega| > \omega_{max} \end{cases}; \omega = -k\chi_e + \frac{\dot{\chi}_d}{\lambda_u(\psi)}; k > 0 \tag{24}$$

It is observed from (24) that, the heading rate controller consist of two main parts: a feedback term $\left(\frac{\dot{\chi}_d}{\lambda_u(\psi)}\right)$ and a feedforward term $(-k\chi_e)$. $k > 0$ represents the feedback gain. By implementing the heading rate controller as shown in (24), the relative course χ of the UAV is indirectly controlled to follow the desired one χ_d generated by the LGVF. Therefore, in order to ensure that χ_d can be followed by the proposed controller, the allowable lower bound of ω_{max} must be determined. Before discussing the allowable lower bound of ω_{max}, Lemma 1 and Lemma 2 are presented.

Lemma 1. *If the airspeed of the UAV is faster than the speed of wind and target, i.e., $v_s^2 \ge T_x^2 + T_y^2$, the following inequality is true.*

$$\frac{v_r}{\lambda_u(\psi)} \le \frac{\left(v_s + \sqrt{T_x^2 + T_y^2}\right)^2}{v_s} \tag{25}$$

Remark 2. *The proof of Lemma 1 is seen in Appendix A. Lemma 1 can be used to determine the bound of $\dot{\chi}_d$ if the heading rate input constraint ω_{max} is provided. The relevant conclusions are shown in Lemma 2.*

Lemma 2. *If the heading rate control law given by (24) is applied to the relative motion model of the UAV as shown in (9), there exists a constant $k_1: 0 < k_1 \le \frac{k}{2}$, such that: ① $\dot{\chi}_d \ge -\lambda_u(\psi)\omega_{max} + k_1 sin\chi_e$, $\chi_e \in [0, \pi)$; ② $\dot{\chi}_d \le \lambda_u(\psi)\omega_{max} + k_1 sin\chi_e$, $\chi_e \in [-\pi, 0)$.*

Remark 3. *The proof of Lemma 2 is seen in Appendix B. Lemma 2 provided the bound of desired heading rate, i.e., $|\dot{\chi}_d - k_1 sin\chi_e| \le \lambda_u(\psi)\omega_{max}$, $\chi_e \in [-\pi, \pi)$.*

Based on Lemma 1 and Lemma 2, the allowable bound of ω_{max} can be determined in Theorem 2.

Preprints (www.preprints.org) | NOT PEER-REVIEWED | Posted: 20 July 2023 doi:10.20944/preprints202307.1347.v1

Theorem 2. *In order to ensure that the UAV successfully perform standoff target tracking by implementing the heading rate controller as shown in (24), and the input signal u always do not violate the heading rate constraint, i.e. $|u| \le \omega_{max}$, the allowable lower bound of ω_{max} must satisfies the following condition.*

$$\omega_{max} \ge \omega_{inf} \triangleq \frac{4\left(v_s + \sqrt{T_x^2 + T_y^2}\right)^2}{v_s r_d} \tag{26}$$

Proof. The proof is discussed in two cases in terms of the relative distance.

a) $r = 0$. According the proposed heading rate control law as shown in Equation (24), when $r = 0$, $\chi_e = 0$. Now, the desired relative course rate is $\dot{\chi}_d = \frac{4v_r}{r_d}$. And then according to Lemma 1, the following can be derived

$$u = \left(\frac{4}{r_d}\right)\left(\frac{v_r}{\lambda_u(\psi)}\right) \le \left(\frac{4}{r_d}\right)\left(\frac{\left(v_s + \sqrt{T_x^2 + T_y^2}\right)^2}{v_s}\right) \triangleq \omega_{inf} \tag{27}$$

It can be observed from Equation (27) that, when $r = 0$, if $\omega_{max} \ge \omega_{inf}$, then $|u| \le \omega_{max}$ is always true. It means that, when $r = 0$, the proposed heading rate control satisfy the input constraint as shown in Equation (3).

b) $r > 0$. According to Lemma 2, the desired heading rate $\dot{\chi}_d$ is bounded, and the following inequations can be derived

$$\begin{aligned} &|\dot{\chi}_d - k_1 sin\chi_e| \le \lambda_u(\psi)\omega_{max} \\ &\Rightarrow \left|\frac{\dot{\chi}_d}{\lambda_u(\psi)} - 2k_1 sin\chi_e\right| \le \omega_{max} \\ &\Rightarrow \left|\frac{\dot{\chi}_d}{\lambda_u(\psi)} - ksin\chi_e\right| \le \omega_{max} \\ &\Rightarrow \left|\frac{\dot{\chi}_d}{\lambda_u(\psi)} - k \cdot \chi_e\right| \le \omega_{max} \\ &\Rightarrow |u| \le \omega_{max} \end{aligned} \tag{28}$$

It can be observed from Equation (28) that, when $r > 0$, $|u| \le \omega_{max}$ is always true. Thus, the proof for Theorem 2 is completed. □

Remark 4. *Theorem 2 provided the formulated inequality between the standoff radius r_d and the maximum heading rate ω_{max} as follows*

$$r_d \ge r_{d,min} \triangleq \frac{4\left(v_s + \sqrt{T_x^2 + T_y^2}\right)^2}{v_s \omega_{max}} \tag{29}$$

In other words, due to the input constraint $|u| \le \omega_{max}$, when the UAV performs the standoff target tracking mission with the constant airspeed v_s, the predefined standoff radius r_d has an allowable lower bound. The minimum allowable standoff radius can be calculated according to Equation (29).

3.3. Stability Analysis of Saturated Heading Control Law

Although Theorem 2 proves that the proposed heading rate control law satisfies the input constraint $|u| \le \omega_{max}$, whether χ converges to χ_d or not will be investigated. In addition, if $\chi_e \to 0$ as $t \longrightarrow +\infty$, the convergence speed of χ_e also needs further discussion. Thus, Lemma 3 is presented.

Lemma 3. *If the UAV described by relative motion model as shown in (9) implements the heading rate control law given by (24), there exists a positive constant $0 < k_2 \le \frac{k}{2} \le k_1$ such that ① $\dot{\chi}_e \ge -k_2 sin\chi_e > 0$, $\chi_e \in [-\pi, 0)$; ② $\dot{\chi}_e \le -k_2 sin\chi_e < 0$, $\chi_e \in [0, \pi)$.*

Remark 5. *The proof of Lemma 3 is seen in Appendix C. According to Lemma 3, it can be derived that*

Preprints (www.preprints.org) | NOT PEER-REVIEWED | Posted: 20 July 2023 doi:10.20944/preprints202307.1347.v1

$$\chi_e\dot{\chi}_e \le -k_2\chi_e sin\chi_e \le 0 \tag{30}$$

Equation (31) shows that, for every initial relative course error $\chi_e(t_0) \in [-\pi,\pi)$, the relative course error $\chi_e \to 0$ as $t \to +\infty$. Thus, the convergence of the proposed heading rate control law is proved in Lemma 3. In addition, Lemma 3 also gives a lower bound on the convergence rate $\dot{\chi}_e$, which is defined as follows

$$|\dot{\chi}_e| \ge |\dot{\chi}_e|_{inf} = k_2|sin\chi_e|, \chi_e \in [-\pi,\pi) \tag{31}$$

By solving the differential inequality shown in (31), the relative course error χ_e varies according to the following inequality

$$\left|tan\left(\frac{\chi_e}{2}\right)\right| \le \left|tan\left(\frac{\chi_e(t_0)}{2}\right)\right| e^{-k_2 t} \tag{32}$$

Equation (32) can be used to analyze the bound of the relative distance r between the UAV and the target. The relevant conclusions are shown in Lemma 4.

Lemma 4. *Given an arbitrary initial relative course error $\chi_e(t_0) \in [-\pi,\pi)$, if the UAV described by relative motion model as shown in (9) implements the heading rate control law given by (24), the relative distance r has an upper bound r_{sup} as follows*

$$r_{sup} = r_0 + \frac{v_s + T}{k_0} ln\left|\frac{tan\left(\frac{\chi_{e0}}{2}\right)}{tan\left(\frac{\alpha_0}{2} - \frac{\pi}{4}\right)}\right| \tag{33}$$

where $T = \sqrt{T_x^2 + T_y^2}$ and $\alpha_0 = arctan\left(\frac{r_0}{r_d}\right)$. The proof of Lemma 4 is seen in Appendix D.

Based on Lemma 3 and Lemma 4, Theorem 3 present a complete proof for the stability of the proposed heading rate control law with control input constrains.

Theorem 3. *Given an arbitrary initial relative course error $\chi_{e0} \in [-\pi,\pi)$, if the UAV described by relative motion model as shown in (9) implements the heading rate control law given by (24), the trajectory of the UAV asymptotically converges to the standoff circle, i.e., $r \longrightarrow r_d$ and $\chi \to \chi_d$ as $t \longrightarrow +\infty$.*

Proof. Let $\mu > 0$, and a Lyapunov function is introduced as follows

$$V = \frac{1}{2}(r - r_d)^2 + \frac{1}{2}\mu\chi_e^2 \tag{34}$$

Differentiating Equation (34) with respect to time t, the outcome is

$$\dot{V} = (r - r_d)\dot{r} + \mu\chi_e\dot{\chi}_e \tag{35}$$

a) If $|\chi_e| \in \left[\frac{\pi}{2},\pi\right]$, according to Lemma 4, we obtain $(r - r_d)\dot{r} = (r - r_d)v_s cos(\chi - \theta) \le (r_{sup} + r_d)(v_s + T)$. And according to Lemma 3, we have $\mu\chi_e\dot{\chi}_e \le \mu\chi_e(-k_2 sin\chi_e) \le \mu\left(\frac{\pi}{2}\right)(-k_2 sin\chi_{e0})$. They yield that

$$\dot{V} \le (r_{sup} + r_d)(v_s + T) - \mu k_2\left(\frac{\pi}{2}\right) sin\chi_{e0} \tag{36}$$

It can be observed that from Equation (36), if $\mu \ge \mu_1 \triangleq \frac{2(r_{sup}+r_d)(v_s+T)}{k_2\pi sin\chi_{e0}}$, then $\dot{V} \le 0$.

b) If $|\chi_e| \in \left[0,\frac{\pi}{2}\right]$, according to Lemma 3, one obtains

$$\mu\chi_e\dot{\chi}_e \le -\mu k_2\chi_e sin\chi_e \tag{37}$$

According to the relative motion model of the UAV as shown in (9), we have

$$\dot{r} = -\left(\frac{r^2 - r_d^2}{r^2 + r_d^2}\right) v_r cos\chi_e - v_r sin\phi_{GF} sin\chi_e \tag{38}$$

Substituting Equation (37) and Equation (38) into Equation (35), it yields that

Preprints (www.preprints.org) | NOT PEER-REVIEWED | Posted: 20 July 2023 doi:10.20944/preprints202307.1347.v1

$$\dot{V} \leq -\frac{(r-r_d)^2(r+r_d)v_r}{r^2+r_d^2}cos\chi_e - v_r(r-r_d)\,sin\phi_{GF}sin\chi_e - \mu k_2\chi_e sin\chi_e \tag{39}$$

For the second term in Equation (39), it holds

$$-v_r(r-r_d)\,sin\phi_{GF}sin\chi_e \leq 2v_r|r-r_d|\left|sin\frac{\chi_e}{2}\right| \tag{40}$$

For the third term in Equation (39), it holds

$$\chi_e sin\chi_e \geq 2sin^2\left(\frac{\chi_e}{2}\right) \tag{41}$$

Substituting Equation (40) and Equation (41) into Equation (39) , it yields that

$$\dot{V} \leq -\frac{(r-r_d)^2(r+r_d)v_r}{r^2+r_d^2} + 2v_r|r-r_d|\left|sin\frac{\chi_e}{2}\right| - 2\mu k_2 sin^2\left(\frac{\chi_e}{2}\right) \tag{42}$$

Solving (42) by completing the square, it is easy to know that, if $\mu \geq \mu_2 \triangleq \frac{(r_{sup}^2+r_d^2)}{k_2(r_{sup}+r_d)}$, then

$$\dot{V} \leq -2\mu k_2 sin^2\left(\frac{\chi_e}{2}\right) - \left\{\left[\frac{(r+r_d)}{r^2+r_d^2}\right]^{\frac{1}{2}}|r-r_d| - \left[\frac{(r^2+r_d^2)}{r+r_d}\right]^{\frac{1}{2}}\left|sin\left(\frac{\chi_e}{2}\right)\right|\right\}^2 \leq 0 \tag{43}$$

Therefore, when $\mu \geq max\{\mu_1, \mu_2\}$, the time derivative of the Lyapunov function is always non-positive, i.e., $\dot{V} \leq 0$. It can be observed from (43) that, $\dot{V} = 0$ implies that $r = r_d$ and $\chi_e = 0$. According to LaSalle's invariance principle, it can be concluded that $r \longrightarrow r_d$ and $\chi \rightarrow \chi_d$ as $t \longrightarrow +\infty$. It means that, the trajectory of the UAV asymptotically converges to the standoff circle. Thus, the proof for Theorem 3 is completed. □

Remark 6. *According to Theorem 3, it is concluded that, by implementing the proposed heading rate control law, the relative distance and the relative course of the UAV are converged to the desired values, respectively. It means that, the control objectives 1 and 2 proposed in Section 2.2 are achieved, and the UAV tracks the moving target while maintaining desired standoff distance successfully.*

4. Cooperative Standoff Tracking Using Multiple UAVs

When a team of UAVs is used to track a ground moving target, coordination between aircraft is necessary to avoid collisions and to maximize sensor coverage of target. A possible solution to this coordination problem is the so-called "phase separation" approach whereby the UAVs fly along the standoff circle with equal intervehicle phase separation angle with respect to its neighbors. Literature [25] proposes a space phase separation algorithm (SPSA) to achieve desired angular spacing as illustrated in Figure 3.

Preprints (www.preprints.org) | NOT PEER-REVIEWED | Posted: 20 July 2023 doi:10.20944/preprints202307.1347.v1

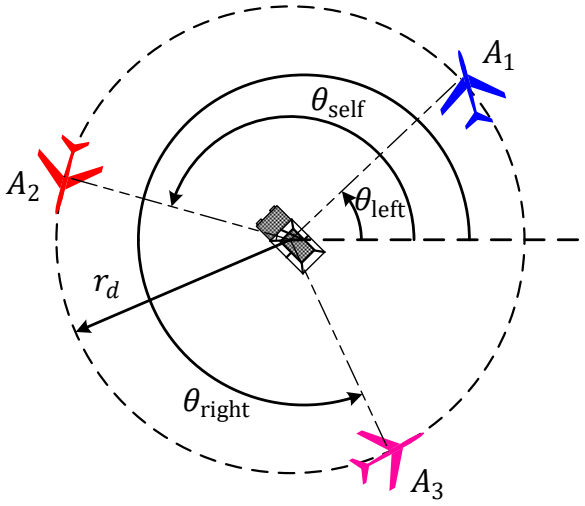

Figure 3. Illustration of phase separation control for UAVs.

As shown in Figure 3, three UAVs are distributed counterclockwise in the standoff circle according to the ascending sequence of their unique identity numbers $A_i(i = 1,2, \dots N)$. Each UAV A_i independently calculates its airspeed control input $v_{s,i}$, based on its own phase angle θ_i, the phase angle $\theta_{\text{left}} = \theta_{i-1}$ of its left neighbor A_{i-1}, and the phase angle $\theta_{\text{right}} = \theta_{i+1}$ of its right neighbor A_{i+1}. For A_1, its left neighbor is A_N and its right neighbor is A_2. For A_N, its left neighbor is A_{N-1} and its right neighbor is A_1.

In [25], the space phase separation angle of A_i, $\Delta\theta_i \in [-\pi, \pi)$, is defined as $\Delta\theta_i = \theta_i - \theta_{\text{left}}$. Similarly, the phase separation angle of the right neighbor A_{i+1} is defined as $\Delta\theta_{\text{right}} = \theta_{\text{right}} - \theta_i$. The space phase separation error of A_i, $e_{\theta,i} \in [-\pi, \pi)$, is defined as $e_{\theta,i} = \Delta\theta_i - \theta_d$. Similarly, the space phase separation error of the right neighbor A_{i+1} is defined as $e_{\theta,\text{right}} = \Delta\theta_{\text{right}} - \theta_d$. Thus, the airspeed control input of A_i can be designed as $v_{s,i} = k_\theta(e_{\theta,\text{right}} - e_{\theta,i})r_i + v_{sd}$. Where $k_\theta > 0$, r_i represents the relative distance between A_i and the target. v_{sd} represents the desired airspeed when the team of UAVs loiter around the target with along a standoff circle synchronously. In this paper, v_{sd} is called standoff speed for short.

However, the SPSA method proposed in [25] has two disadvantages. (i) The airspeed limitation as shown in Equation (2) is not considered in SPSA; (ii) The space phase separation $\Delta\theta_i$ and corresponding error $e_{\theta,i}$ are wrapped in $[-\pi, \pi)$, and thus they are discontinuous. This discontinuity will lead to the oscillation of airspeed control input, and then result in a poor tracking performance of the UAVs. This shortcoming has been confirmed in simulation results of Figure 9 in [25]. In order to avoid the discontinuity of space phase angle, the space phase is replaced by a new notion called temporal phase, which can be also used to represent the distribution of the UAVs on the standoff circle. Based on the temporal phase, a new temporal phase separation algorithm (TPSA) is proposed to achieve desired temporal phase separation in cooperative standoff target tracking mission.

4.1. Airspeed Controller Design for Temporal Phase Separation

In SPSA method, the angle θ_i is utilized to represent the space phase of the UAV A_i. The space phase describes the distribution of the UAVs which keep a circle around the target. Similarly, we can also introduce temporal phase to equivalently describe the distribution of the UAVs. The temporal phase of A_i is defined as follows

$$\tau_i(\theta_i) = \begin{cases} \dfrac{2\pi}{T_\tau}\left[\displaystyle\int_0^{\theta_i+2\pi}\left(\frac{r_d}{v_{rd}}\right)d\theta\right] - \pi, \text{if } \theta_i \in [-\pi, 0) \\ \dfrac{2\pi}{T_\tau}\left[\displaystyle\int_0^{\theta_i}\left(\frac{r_d}{v_{rd}}\right)d\theta\right] - \pi, \qquad \text{if } \theta_i \in [0, \pi) \end{cases} \tag{44}$$

Preprints (www.preprints.org) | NOT PEER-REVIEWED | Posted: 20 July 2023 doi:10.20944/preprints202307.1347.v1

where $\tau_i(\theta_i) \in [-\pi, \pi)$ represents temporal phase of A_i. v_{rd} is the desired relative speed of A_i with respect to the target, and can be expressed as follows.

$$v_{rd} = \left[v_{sd}^2 + T_x^2 + T_y^2 - 2v_{sd}(T_x cos\psi_d + T_y sin\psi_d)\right]^{\frac{1}{2}} \tag{45}$$

where ψ_d represents the desired heading when A_i flies along the standoff circle.

$$\psi_d = arcsin\left(\frac{T_y cos\chi_d - T_x sin\chi_d}{v_{sd}}\right) + \chi_d \tag{46}$$

In Equation (44), T_τ represents the time required for the UAV to complete a circle of flight along the standoff circle with the desired airspeed v_{sd}. T_τ is used to normalized the flight time of the UAV, and is defined as $T_\tau = \int_0^{2\pi}\left(\frac{r_d}{v_{rd}}\right)d\theta$. It can be observed from (44) that, the temporal phase $\tau_i(\theta_i)$ represents the normalized time required for the UAV A_i to fly from space phase angle 0 to the current space phase angle θ_i along the standoff circle.

Therefore, the temporal phase separation between A_i and its neighbor is defined by the difference of their temporal phase.

$$\tau_{i-1,i} = \tau_{i-1} - \tau_i \tag{47}$$

Suppose there are $N(N \geq 2)$ UAVs, a leader-follower formation strategy is used in this paper. Without loss of generality, it assumes that A_1 is the leader and its airspeed is the desired one, e.g., $v_{s,1} = v_{sd}$, and is held constant. Then, A_2 follows A_1, and adjusts its airspeed to achieve the desired temporal separation with its leader A_1. Similarly, A_i follows its leader A_{i-1}, and achieves the desired temporal separation by varying its airspeed. The temporal separation error is defined as follows

$$\Delta\tau_i = \tau_{i-1} - \tau_i - \tau_d \tag{48}$$

where τ_d represents the desired separation. The airspeed input is designed as follows

$$\begin{cases} v_{s,1} = v_{sd} \\ v_{s,i} = v_{sd} + \left(\frac{\Delta v \cdot \Delta\tau_i}{\pi}\right)\left(\frac{r_{i-1}^2 + r_d^2}{r_{i-1}^2 + r_i^2}\right), i > 1 \end{cases} \tag{49}$$

where $\Delta v > 0$ represents the airspeed increment of the UAV in one time step, and it reflects the performance of the onboard autopilot.

Before verifying that the proposed controller (49) always satisfy the min and max airspeed constraint (2), Assumption 5 is introduced as follows:

Assumption 5. *There exists appropriate values of v_{sd} and Δv, so that the following constraints are satisfied, $v_{sd} - \Delta v > \sqrt{T_x^2 + T_y^2}$ and $v_{min} + \Delta v \leq v_{sd} \leq v_{max} - \Delta v$.*

Remark 7. *Generally speaking, the airspeed of the UAV is always faster than the target speed and the wind speed, thus the constraint, $v_{sd} - \Delta v > \sqrt{T_x^2 + T_y^2}$, could be satisfied. In addition, the Δv is depended on the performance of the autopilot, which definitely satisfies the requirement of $v_{min} + \Delta v \leq v_{sd} \leq v_{max} - \Delta v$. Therefore, Assumption 5 is reasonable. Based on Assumption 5, the following Theorem 4 is proposed.*

Theorem 4. *If the standoff speed v_{sd} and the speed increment Δv are satisfy the inequality conditions presented in Assumption 5, then the proposed controller given by (49) always satisfy the min and max airspeed constraint given by (2).*

Proof. According to (49), let $= v_{s,i} - v_{sd} = \Delta v \cdot \alpha \cdot \beta$, where $\alpha = \frac{\Delta\tau_i}{\pi}$ and $\beta = \frac{r_{i-1}^2 + r_d^2}{r_{i-1}^2 + r_i^2}$. Due to $\Delta\tau_i \in [-\pi, \pi)$, then $|\Delta\tau_i| \leq \pi$ and $|\alpha| \leq 1$. If $r_i \geq r_d$, then $0 < \beta \leq 1$, i.e., $|\beta| \leq 1$.

$$|\gamma| = \Delta v \cdot |\alpha| \cdot |\beta| \leq \Delta v \tag{50}$$

Considering $v_{s,i} = v_{sd} + \gamma$, it yields that

Preprints (www.preprints.org) | NOT PEER-REVIEWED | Posted: 20 July 2023 doi:10.20944/preprints202307.1347.v1

$$v_{sd} - |\gamma| \le \left(|v_{s,i}| = |v_{sd} + \gamma|\right) \le v_{sd} + |\gamma| \tag{51}$$

Substituting Equation (50) into Equation (51), it yields that

$$v_{sd} - \Delta v \le |v_{s,i}| \le v_{sd} + \Delta v \tag{52}$$

According to Assumption 5, it is obtained that, $v_{min} \le v_{sd} - \Delta v \le |v_{s,i}| \le v_{sd} + \Delta v \le v_{max}$, which implied that $0 < v_{min} \le v_{s,i} \le v_{max}$. Therefore, it can be concluded that the proposed airspeed control law given by Equation (49) always satisfy the min and max airspeed constraint given by Equation (2). Thus, the proof for Theorem 3 is completed. □

4.2. Stability Analysis of Airspeed Control Law

Stability analysis of airspeed control law is provided in the following Theorem 5.

Theorem 5. *For the relative motion model of UAV described in (9) if the heading rate control law given by Equation (24) and the cooperative airspeed control laws given by Equation (49) are applied to a team of UAVs, then each aircraft A_i can achieve equal temporal separation and fly along the standoff circle, i.e. as $t \longrightarrow +\infty$, $\Delta\tau_i \longrightarrow 0$, $i = 2,3,\dots,N$.*

Proof. Differentiating Equation (48) with respect to time t, it yields that

$$\Delta\dot{\tau}_i = \dot{\tau}_{i-1} - \dot{\tau}_i = \left(\frac{2r_d\pi}{T_\tau}\right)\left[\left(\frac{\dot{\theta}_{i-1}}{v_{rd,(i-1)}}\right) - \left(\frac{\dot{\theta}_i}{v_{rd,i}}\right)\right] \tag{53}$$

According to the relative motion model given by Equation (9), one obtains

$$\dot{\theta}_i = \frac{v_{r,i}}{r_i} sin\phi_{GF,i} = \frac{v_{r,i}}{r_i} \cdot \frac{2r_i r_d}{r_i^2 + r_d^2} \tag{54}$$

Suppose that the aircraft A_i $(i = 2,3,\dots,N)$ implementing the proposed heading rate control law given by (24) has been converged on the standoff circle, i.e., $r_i = r_d$. Therefore,

$$\Delta\dot{\tau}_i = \left(-\frac{2\pi}{T_\tau}\right)\left[\frac{v_{r,i} - v_{rd,i}}{v_{rd,i}} - \frac{v_{r,(i-1)} - v_{rd,(i-1)}}{v_{rd,(i-1)}}\right] \tag{55}$$

Let $\sigma = T_x cos\psi_{rd,i} + T_y sin\psi_{rd,i}$, we obtain

$$v_{r,i}^2 - v_{rd,i}^2 = \left(v_{s,i} - v_{sd}\right)\left(v_{s,i} + v_{sd} - 2\sigma\right) \tag{56}$$

According to the cooperative airspeed control laws given by (49), one has

$$v_{s,i} - v_{sd} = \left(\frac{\Delta v \cdot \Delta\tau_i}{\pi}\right) \tag{57}$$

Substituting Equation (57) into Equation (56), it yields that

$$v_{r,i} - v_{rd,i} = K_i \Delta\tau_i \tag{58}$$

where $K_i \triangleq \frac{\Delta v(v_{s,i} + v_{sd} - 2\sigma)}{\pi(v_{r,i} + v_{rd,i})}$. Substituting (58) into (55) and setting $v_{r,1} = v_{rd,1}$, it yields that

$$\begin{cases} \Delta\dot{\tau}_2 = -\dfrac{2\pi}{T_\tau}\left(\dfrac{K_2\Delta\tau_2}{v_{rd,2}} - 0\right) \\ \Delta\dot{\tau}_3 = -\dfrac{2\pi}{T_\tau}\left(\dfrac{K_3\Delta\tau_3}{v_{rd,3}} - \dfrac{K_2\Delta\tau_2}{v_{rd,2}}\right) \\ \vdots \\ \Delta\dot{\tau}_i = -\dfrac{2\pi}{T_\tau}\left(\dfrac{K_i\Delta\tau_i}{v_{rd,i}} - \dfrac{K_{(i-1)}\Delta\tau_{(i-1)}}{v_{rd,(i-1)}}\right) \end{cases} \tag{59}$$

Let $\Delta\boldsymbol{\tau} = (\Delta\tau_2, \Delta\tau_3, \dots, \Delta\tau_N)^{\mathrm{T}}$ and $\varepsilon_i = \frac{2\pi K_i}{T_\tau v_{rd,i}}$, one derives

Preprints (www.preprints.org) | NOT PEER-REVIEWED | Posted: 20 July 2023 doi:10.20944/preprints202307.1347.v1

$$\Delta\dot{\boldsymbol{\tau}} = -\begin{bmatrix} \varepsilon_2 & 0 & \cdots & \cdots \\ -\varepsilon_2 & \varepsilon_3 & 0 & \cdots \\ \vdots & -\varepsilon_3 & \ddots & 0 \\ \vdots & \vdots & -\varepsilon_{N-1} & \varepsilon_N \end{bmatrix}\Delta\boldsymbol{\tau} \tag{60}$$

It is easy to prove that the cascade connected system shown in (60) is asymptotically stable, i.e., $\Delta\boldsymbol{\tau} \longrightarrow \mathbf{0}$ as $t \longrightarrow +\infty$. Thus, the proof for Theorem 5 is completed. □

5. Estimator for the Composition Velocity of Background Wind and Target Motion

In the previous section, the proofs and analyses are based on the assumption that the composition velocity is accurately known a prior. However, in practical applications, this assumption is not always true. Therefore, in this section, an estimator is proposed to estimate the composition velocity in real time.

5.1. The Composition Velocity Estimator Design

Suppose that the composition velocity $\boldsymbol{T} = (T_x, T_y)$ is bounded, and its upper bound is known a prior, denoted as $T^* = sup_{t\geq 0}\{\|\boldsymbol{T}\|_2\}$. According to [31], the target motion and wind are regarded as an external disturbance. And the composition velocity of the external disturbance can be expressed in the form of a hyperbolic tangent function as follows

$$T_x = T^*\tanh\varphi_x; T_y = T^*\tanh\varphi_y \tag{61}$$

The parameters of the external disturbance, φ_x and φ_y, are regarded as estimated variables to obtain the estimated results of the composition velocity. $\hat{\boldsymbol{T}} = (\hat{T}_x, \hat{T}_y)$ is introduced to denote the estimation of (T_x, T_y), then it also can be expressed in the form of a hyperbolic tangent function as follows

$$\hat{T}_x = T^*\tanh\hat{\varphi}_x; \hat{T}_y = T^*\tanh\hat{\varphi}_y \tag{62}$$

where $(\hat{\varphi}_x, \hat{\varphi}_y)$ is an estimate result of the external disturbance parameters. Thus, our goal is to design an estimator which can guarantee that the estimate disturbance parameters can asymptotically coverage to the true values, i.e., $(\hat{\varphi}_x, \hat{\varphi}_y) \rightarrow (\varphi_x, \varphi_y)$ as $t \longrightarrow +\infty$.

Therefore, the dynamics of the estimated relative position are formulated as follows

$$\dot{\hat{x}}_r = v_{sd}cos\psi - \hat{T}_x + k_3\tilde{x}_r; \dot{\hat{y}}_r = v_{sd}sin\psi - \hat{T}_y + k_3\tilde{y}_r \tag{63}$$

where $k_3 > 0$ is a positive constant. $(\tilde{x}_r, \tilde{y}_r)$ is the estimate error of the relative position

$$\tilde{x}_r = x_r - \hat{x}_r; \tilde{y}_r = y_r - \hat{y}_r \tag{64}$$

where $(\hat{x}_r, \hat{y}_r)$ represents the estimated relative position. Then, differentiating (64) with respect to time t, and according to (63), the dynamics of the relative position estimate error can be expressed as follows

$$\dot{\tilde{x}}_r = -\tilde{T}_x - k_3\tilde{x}_r; \dot{\tilde{y}}_r = -\tilde{T}_y - k_3\tilde{y}_r \tag{65}$$

where $(\tilde{T}_x, \tilde{T}_y)$ represents the estimate error of the composition velocity

$$\tilde{T}_x = T_x - \hat{T}_x; \tilde{T}_y = T_y - \hat{T}_y \tag{66}$$

It is worth noting that the errors $(\tilde{T}_x, \tilde{T}_y)$ could be reduced by $(\hat{\varphi}_x, \hat{\varphi}_y)$. Therefore, let $k_4 > 0$ is a positive constant, $(\hat{\varphi}_x, \hat{\varphi}_y)$ is updated as follows

$$\dot{\hat{\varphi}}_x = -k_4\tilde{x}_r; \dot{\hat{\varphi}}_y = -k_4\tilde{y}_r \tag{67}$$

The pseudocode of the composition velocity estimation algorithm (CVEA) is illustrated in **Error! Reference source not found.**.

Preprints (www.preprints.org) | NOT PEER-REVIEWED | Posted: 20 July 2023 doi:10.20944/preprints202307.1347.v1

Algorithm 1 Pseudocode of the composition velocity estimation algorithm (CVEA)

Input: The estimate results $\left[\hat{T}_x^{\ominus}, \hat{T}_y^{\ominus}, \hat{\varphi}_x^{\ominus}, \hat{\varphi}_y^{\ominus}, \hat{x}_r^{\ominus}, \hat{y}_r^{\ominus}\right]^{\mathrm{T}}$ at time t_{k-1}, and the measured relative position $[x_r, y_r]^{\mathrm{T}}$ at the present t_k.

Output: The estimate results $\left[\hat{T}_x^{\oplus}, \hat{T}_y^{\oplus}, \hat{\varphi}_x^{\oplus}, \hat{\varphi}_y^{\oplus}, \hat{x}_r^{\oplus}, \hat{y}_r^{\oplus}\right]^{\mathrm{T}}$ at time t_k.

1. Update the estimate error of the relative position by the following equations

$$\tilde{x}_r = x_r - \hat{x}_r^{\ominus}; \tilde{y}_r = y_r - \hat{y}_r^{\ominus}$$

where, (x_r, y_r) can be regarded as the measurement update at time t_k; $(\hat{x}_r^{\ominus}, \hat{y}_r^{\ominus})$ represent the prior estimation of the relative position at time t_{k-1}.

2. Calculate a posterior estimate of the external disturbance parameters (φ_x, φ_y) as follows

$$\hat{\varphi}_x^{\oplus} = \hat{\varphi}_x^{\ominus} - k_4 \tilde{x}_r \cdot \Delta t; \hat{\varphi}_y^{\oplus} = \hat{\varphi}_y^{\ominus} - k_4 \tilde{y}_r \cdot \Delta t$$

where $\Delta t = t_k - t_{k-1}$ represents the time step.

3. A posteriori estimation of the composition velocity (T_x, T_y) is calculated as follows

$$\hat{T}_x^{\oplus} = T^* \tanh \hat{\varphi}_x^{\oplus}; \hat{T}_y^{\oplus} = T^* \tanh \hat{\varphi}_y^{\oplus}$$

4. Update the posterior estimate of the relative position by the following equations

$$\hat{x}_r^{\oplus} = \hat{x}_r^{\ominus} + \left(v_{sd} cos\psi - \hat{T}_x^{\oplus} + k_3 \tilde{x}_r\right)\Delta t; \hat{y}_r^{\oplus} = \hat{y}_r^{\ominus} + \left(v_{sd} sin\psi - \hat{T}_y^{\oplus} + k_3 \tilde{y}_r\right)\Delta t$$

5. Update time $t_{k-1} \leftarrow t_k$, go to Step 1 to start the next round of estimation.

Figure 4. Pseudocode of the composition velocity estimation algorithm (CVEA).

It is worth explaining that the differences between the CVEA proposed in this paper and literature [31] are shown in **Error! Reference source not found.**. As shown in **Error! Reference source not found.**, point A represents the current position of the UAV, the corresponding azimuth angle is denoted by θ. Suppose P is the point with the corresponding azimuth angle θ on the desired obit of the LGVF, and the position of P can be calculated according to Equation (16). Generally speaking, it is hoped that the two points A and P should be coincide. However, due to the effect of external disturbance, there exists an offset between the actual vehicle trajectory and the desired LGVF orbit, denoted as $\tilde{\boldsymbol{r}}(\theta) = \overrightarrow{AP} = (\tilde{x}_r, \tilde{y}_r)$. The offset can be used to estimate the composition velocity. In this paper, the CVEA approach uses the whole offset vector $[\tilde{x}_r, \tilde{y}_r]^{\mathrm{T}}$ to obtain the estimation of the composition velocity. But literature [31] only uses the radial distance of offset, i.e., $\tilde{r}(\theta) = \sqrt{\tilde{x}_r^2 + \tilde{y}_r^2}$, in the estimator. Theoretically speaking, because the feedback item contains more information, comparing with literature [31], the composition velocity can be estimated faster and more accurately in the proposed CVEA.

Preprints (www.preprints.org) | NOT PEER-REVIEWED | Posted: 20 July 2023 doi:10.20944/preprints202307.1347.v1

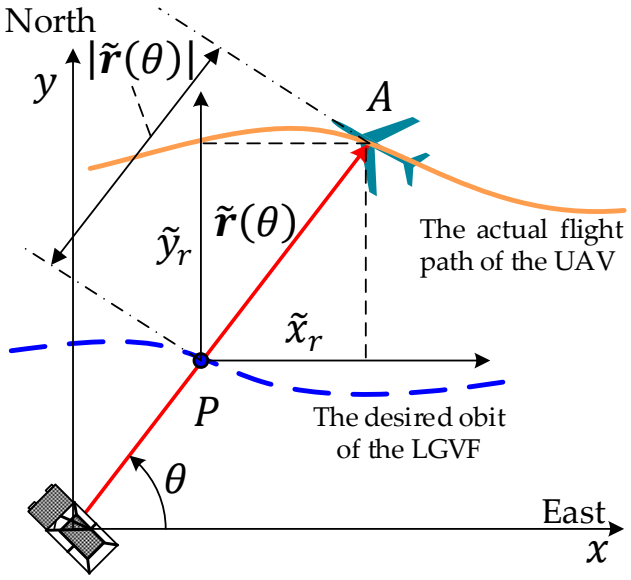

Figure 5. Principle of CVEA.

5.2. Convergence Analysis of the Composition Velocity Estimator

Convergence analysis of the composition velocity estimator is provided in the following Theorem 6.

Theorem 6. *The composition velocity estimator given by Equation (63)-(67) is asymptotically stable, i.e.* $\hat{T}_x \to T_x$ *and* $\hat{T}_y \to T_y$ *as* $t \longrightarrow +\infty$.

Proof. Consider the following the Lyapunov function

$$V = \frac{1}{2}\tilde{x}_r^2 + \frac{1}{2}\tilde{y}_r^2 + \frac{T^*}{k_4}\left[\ln\left(\cosh(\hat{\varphi}_x)\right) - \hat{\varphi}_x \cdot \tanh(\varphi_x)\right] + \frac{T^*}{k_4}\left[\ln\left(\cosh(\hat{\varphi}_y)\right) - \hat{\varphi}_y \cdot \tanh(\varphi_y)\right] \tag{68}$$

(a) Firstly, we prove that the Lyapunov function V is negative semi-definite, i.e., $\dot{V} \leq 0$.

Differentiating (68) with respect to time t, and according to Equations (63)-(67), it yields that

$$\dot{V} = \tilde{x}_r\dot{\tilde{x}}_r + \tilde{y}_r\dot{\tilde{y}}_r - \frac{\dot{\hat{\varphi}}_x}{k_4}\tilde{T}_x - \frac{\dot{\hat{\varphi}}_y}{k_4}\tilde{T}_y = -k_3(\tilde{x}_r^2 + \tilde{y}_r^2) \leq 0 \tag{69}$$

(b) Secondly, it is shown that the Lyapunov function V is lower bounded, i.e., $V \geq V_{inf}$.

An assistant function is defined as $H(x) = ln\left(cosh(x)\right) - x \cdot tanh(x_0)$. Differentiating $H(x)$ with respect to x, we obtain $\frac{\partial H}{\partial x} = \tanh(x) - \tanh(x_0)$. It means that when $x = x_0$, $H(x)$ reaches the minimum, i.e. $H(x) \geq H(x_0) \geq -ln2$. Thus, when $\hat{\varphi}_x = \varphi_x$ and $\hat{\varphi}_y = \varphi_y$, the Lyapunov function V reaches the following lower bounded $V \geq V_{inf} \triangleq -\frac{2T^*}{k_4}\ln 2$. Therefore, the function V is lower bounded.

(c) At last, we prove that the function $\ddot{V}$ is bounded.

Differentiating Equation (69) with respect to time t, one obtains

$$\ddot{V} = -2k_3\left(\tilde{x}_r \cdot \dot{\tilde{x}}_r + \tilde{y}_r \cdot \dot{\tilde{y}}_r\right) = 2k_3\left[\tilde{x}_r\left(\tilde{T}_x + k_3\tilde{x}_r\right) + \tilde{y}_r\left(\tilde{T}_y + k_3\tilde{y}_r\right)\right] \tag{70}$$

Because $\tilde{x}_r$, $\tilde{y}_r$, $\tilde{T}_x$, $\tilde{T}_y$ are both bounded in proposed estimator, thus the function $\ddot{V}$ is also bounded. Therefore, according to Barbalat's lemma, it is concluded that, $\dot{V} \to 0$ as $t \longrightarrow +\infty$. It implies that, $\tilde{x}_r \to 0$ and $\tilde{y}_r \to 0$ as $t \longrightarrow +\infty$. In addition, it can be proved that $\dot{\tilde{x}}_r$ is also bounded, and thus we can conclude that $\dot{\tilde{x}}_r = -\tilde{T}_x - k_3\tilde{x}_r \to 0$ according to Barbalat's lemma. In other words,

Preprints (www.preprints.org) | NOT PEER-REVIEWED | Posted: 20 July 2023 doi:10.20944/preprints202307.1347.v1

$\tilde{T}_x \to 0$. Similarly, it can also be proved that $\tilde{T}_y \to 0$. We can summarize that, $\hat{T}_x \to T_x$ and $\hat{T}_y \to T_y$ as $t \longrightarrow +\infty$. Thus, the proof for Theorem 6 is completed. □

6. Simulation Results

Firstly, in Section 6.1, scenario 1 that contained two UAVs and a single target is used to verify the feasibility of the cooperative standoff target tracking algorithm (CSTTA) in unknown background wind.

Secondly, to verify the performance of the CVEA, the simulation results of the CVEA approach is compared with that of the method in literature [31]. In Section 6.2, the comparative experiments are carried out in scenario 2 that contained a single UAV and a target.

Finally, Section 6.3 presents scenario 3 that contained three UAVs and a single target. The performance of the proposed TPSA and the SPSA method presented in literature [25] are compared to verify the TPSA has smaller separation errors and faster convergence rate.

6.1. Scenario 1: Tracking a Moving Target Using Two UAVs

In scenario 1, two UAVs are used to perform cooperative standoff tracking mission of a ground moving target in unknown background wind. The simulation conditions for scenario 1 are shown in Table 1. The kinematic constraints of the UAV are shown in Table 2. Due to the ground target move with much lower speeds than UAVs, the constant-velocity target model is used in simulations. The target performs approximately uniform linear motion, but the target velocity will be slight changed due to noise. Tables 3 and 4 list the initial settings of the UAVs and target respectively.

Table 1. Simulation conditions (scenario 1).

Parameter	Description	Value
t_0	Initial time of simulation	0s
Δt	Sampling time	1.0s
t_f	Final time of simulation	400s
(w_x, w_y)	Wind velocity	(-5, -2) m/s
T^*	Upper bound	10m/s
v_{sd}	Desired standoff airspeed	100m/s
r_d	Desired standoff radius	1000m

Table 2. Kinematic constraints of the UAV (scenario 1).

Parameter	Description	Value
v_{min}	Allowable minimum airspeed	60m/s
v_{max}	Allowable maximum airspeed	160m/s
Δv	Unit increment of airspeed	30m/s
ω_{max}	Maximum heading rate	30deg/s

Table 3. The initial settings of target (scenario 1).

Parameter	Description	Value
(x_t, y_t)	Initial position of target	(-10, 0) m
$(\dot{x}_t, \dot{y}_t)$	Initial velocity of target	(2, 3) m/s
(δ_x, δ_y)	Process noise covariance of target	(0.1, 0.1) m/s^2

On one hand, according to Theorem 2 in section 3.2, if v_{sd}=100m/s, (T_x, T_y) = (7,5) m/s, ω_{max}=0.524rad/s, the minimum allowable standoff radius is $(r_d)_{inf}$=829.7218m. The desired standoff distance r_d=1000m > $(r_d)_{inf}$ will satisfy the heading rate constraints. On other hand, if the wind velocity is (w_x, w_y) = (-5, -2) m/s, and the target velocity is $(\dot{x}_t, \dot{y}_t)$ = (2, 3) m/s, then the composition velocity is (T_x, T_y) = (7, 5) m/s. When v_{sd} = 100m/s, v_{min} = 60m/s, v_{max} = 160m/s, Δv = 30m/s, it

Preprints (www.preprints.org) | NOT PEER-REVIEWED | Posted: 20 July 2023 doi:10.20944/preprints202307.1347.v1

is verified that the conditions $v_{sd} - \Delta v > \sqrt{T_x^2 + T_y^2}$ and $v_{min} + \Delta v \le v_{sd} \le v_{max} - \Delta v$ are satisfied. According to Theorem 4 in section 4.1, the simulation conditions in scenario 1are satisfy the input constraints of the UAV.

Table 4. The initial settings of UAVs (scenario 1).

UAV A_i	Position(x_i, y_i)/m	Velocity v_i/(m/s)	Heading ψ_i/(deg)
A_1	(700, 400)	100	135
A_2	(-1200, 600)	100	20

The trajectories of UAVs and target in inertial frame are shown in Figure 6. The black solid line represents the target's trajectory, the red dot line represents the trajectory of A_1, and the blue dash-dot line represents the trajectory of A_2. The triangular arrow "△" indicates the heading ψ of the UAV. The black arrow "→" indicates the wind velocity.

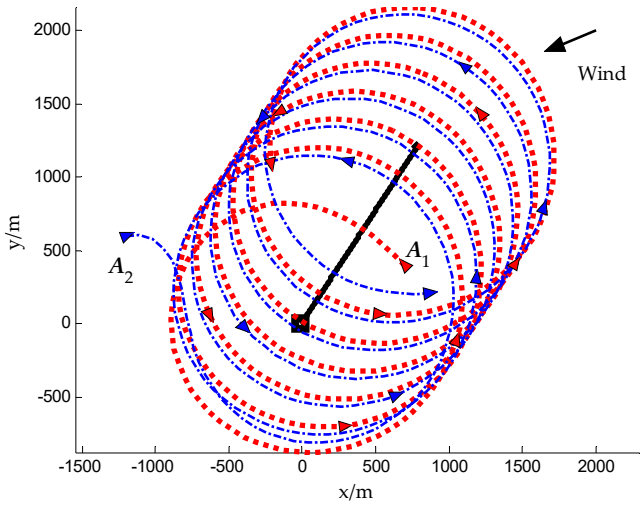

Figure 6. Trajectories of UAVs and target in inertial coordinates (scenario 1).

The trajectories of UAVs in local target frame coordinates are shown in Figure 7, and the triangular arrow "△" represents the relative course χ of the UAV. The UAVs initially have arbitrary position and heading, and are eventually steered to loiter around the target with predefined standoff distance r_d = 1000m. Meanwhile, the UAVs are converged to the desired relative course along the LGVF. In addition, the UAVs achieve the desired phase separation when all vehicles arrive at the standoff circle.

Preprints (www.preprints.org) | NOT PEER-REVIEWED | Posted: 20 July 2023 doi:10.20944/preprints202307.1347.v1

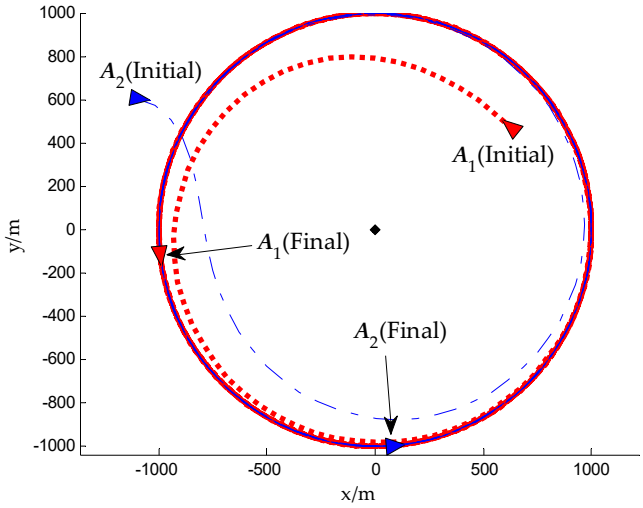

Figure 7. Trajectories of UAVs in local target frame coordinates (scenario 1).

The heading rate control input u and airspeed control input v_s are shown in Figure 8 and Figure 9 respectively. It can be seen that $|u_i| \le \omega_{max}$ and $v_{min} \le v_{s,i} \le v_{max} (i = 1,2)$. It implies that the proposed heading rate controller and airspeed controller are both satisfied the kinematic constraints of the UAV. The simulation results confirm the conclusions of Theorem 2 and Theorem 4.

The estimate results of the composition velocity, $(\hat{T}_x, \hat{T}_y)$, are shown in Figure 10. And the corresponding estimate errors $(\tilde{T}_x, \tilde{T}_y)$ are presented in Figure 11. In order to show more clearly the curves of $(\hat{T}_x, \hat{T}_y)$ and $(\tilde{T}_x, \tilde{T}_y)$, Figures 10 and 11 only plot the histories of $(\hat{T}_x, \hat{T}_y)$ and $(\hat{T}_x, \hat{T}_y)$ in the time period (0-16)s. It can be seen that the estimate errors converge to 0 at about 8s. It implies that the proposed estimator can velocity estimator can obtain stable and accurate estimates of the composition velocity.

The relative distance $r_i (i = 1,2)$ betweenA_1, A_2 and the target is shown in Figure 12. It can be seen that the relative distances of A_1 and A_2 converge to the desired standoff radius r_d = 1000m. The phase separation angle $\Delta\theta = \theta_2 - \theta_1$ is shown in Figure 13. It can be seen that the phase separation angle $\Delta\theta$ eventually converges to 90°. It implies that the optimal observation configuration of the UAVs is generated and maintained. Therefore, the simulation results in scenario 1 verify that the performance of the proposed CSTTA approach. The CSTTA approach can guarantee that the UAVs perform coordinated standoff tracking of a ground moving target in unknown background wind successfully.

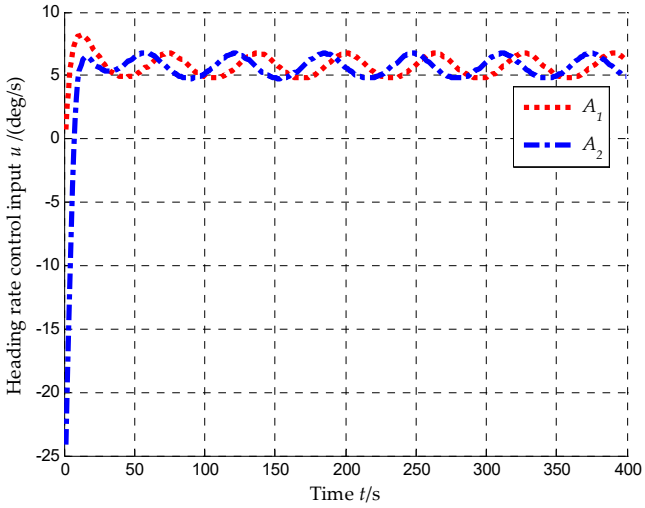

Figure 8. Heading rate control inputs of UAVs, u, (scenario 1).

Preprints (www.preprints.org) | NOT PEER-REVIEWED | Posted: 20 July 2023 doi:10.20944/preprints202307.1347.v1

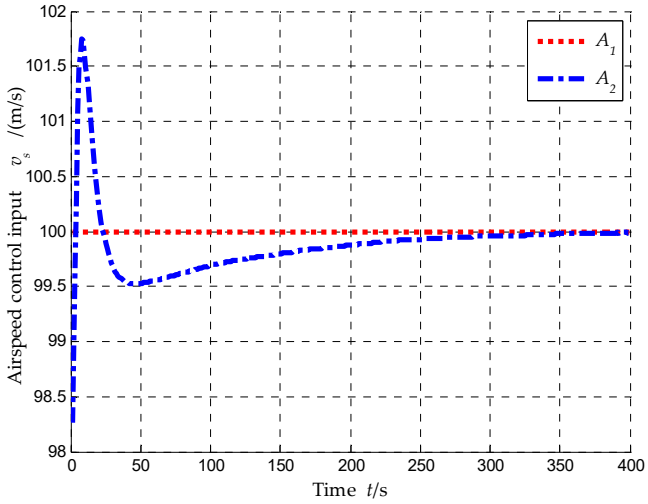

Figure 9. Airspeed control inputs of UAVs, v_s, (scenario 1).

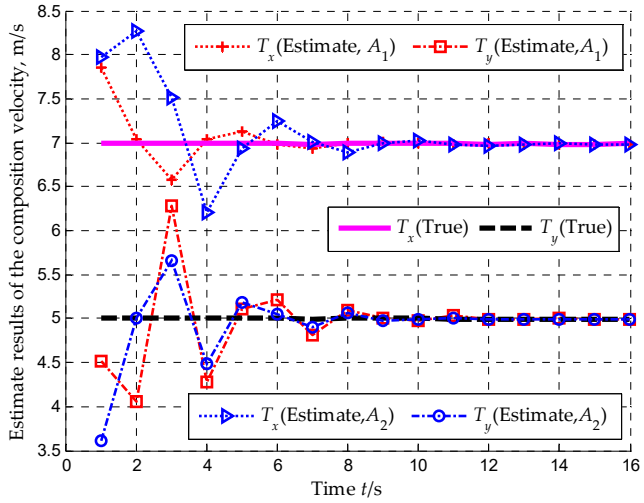

Figure 10. Estimate results of the composition velocity, $(\hat{T}_x, \hat{T}_y)$, (scenario 1).

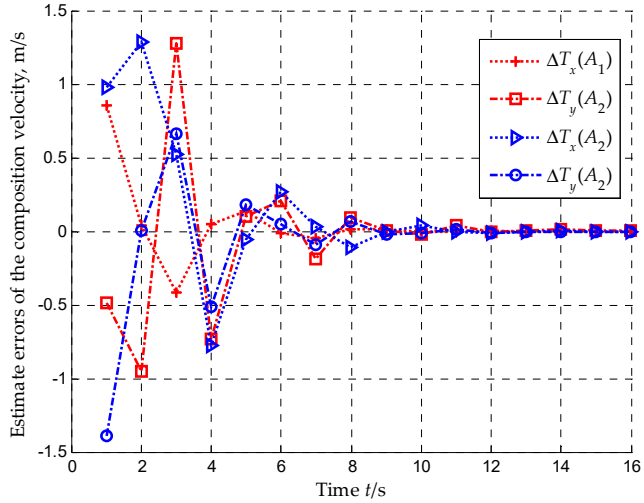

Figure 11. Estimate errors of the composition velocity, $(\tilde{T}_x, \tilde{T}_y)$, (scenario 1).

Preprints (www.preprints.org) | NOT PEER-REVIEWED | Posted: 20 July 2023 doi:10.20944/preprints202307.1347.v1

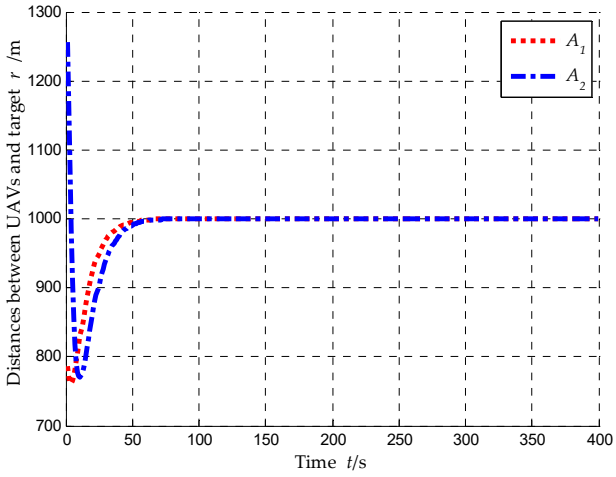

Figure 12. Distances between UAVs and target, r, (scenario 1).

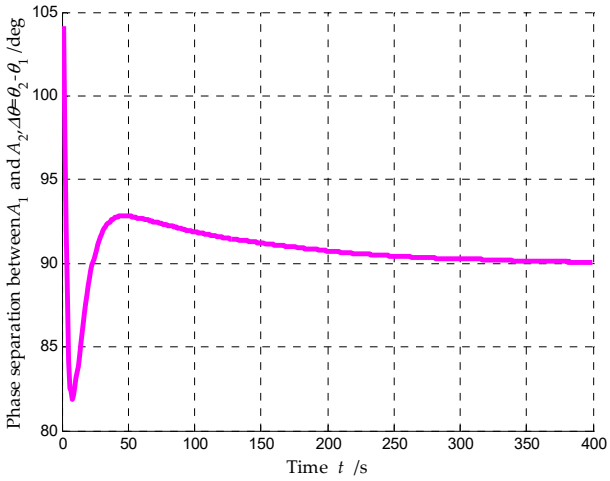

Figure 13. Phase separation between A_1 and A_2, $\Delta\theta = \theta_2 - \theta_1$, (scenario 1).

6.2. Scenario 2: Tracking a Moving Target Using a Single UAV

In scenario 2, a single UAV A_1 is used to execute standoff target tracking mission. The initial settings of A_1 are listed in Table 5, and other simulation conditions are same to scenario 1. In order to verify that the proposed CVEA can generate effective and accurate composition velocity estimation to effectively improve the standoff tracking performance, the simulation results of the single drone's standoff target tracking algorithm (STTA) as shown in Equation (24) with CVEA (denoted as "STTA+CVEA") are compared with that of the method in literature [31].

Table 5. The initial settings of UAVs (scenario 2).

UAV A_i	Position(x_i, y_i)/m	Velocity v_i/(m/s)	Heading ψ_i/(deg)
A_1	(600, 200)	100	90

Firstly, we need to define several performance indexes to evaluate the effectiveness of the CVEA approach and the method in literature [31]. Thus, the global average errors (GAEs) are introduced. It is worth noting that global means it is averaged over the N UAVs. This definition is not only be appropriate for the scenario of a single UAV, but also be appropriate for the scenario of multiple UAVs. At time t_k, the GAE of relative distance regulation is defined as $e_r(t_k) = \frac{1}{N}\sum_{i=1}^{N}|r_i(t_k) - r_d|$. Similarly, the GAE of relative course tracking is defines as $e_\chi(t_k) = \frac{1}{N}\sum_{i=1}^{N}\left|\chi_i(t_k) - \chi_i^d(t_k)\right|$; the GAE of phase separation is defined as $e_\theta(t_k) = \frac{1}{N}\sum_{i=1}^{N}\left|\theta_j(t_k) - \theta_i(t_k) - \theta_d\right|$; the GAE of composition

Preprints (www.preprints.org) | NOT PEER-REVIEWED | Posted: 20 July 2023 doi:10.20944/preprints202307.1347.v1

velocity estimation is defined as $e_T(t_k) = \frac{1}{N}\sum_{i=1}^{N}\left(\tilde{T}_x^2 + \tilde{T}_y^2\right)^{\frac{1}{2}}$. The GAEs can be used to analyze the convergence of the designed controllers and estimator, including the heading rate controller proposed in Section 3.2, the airspeed controller proposed in Section 4.1, and the composition velocity estimator proposed in Section 5.1.

Then, in order to analyze the convergence rate of the designed controllers and estimator, the integrated time absolute error (ITAE) is defined as follows

$$J_{\mathrm{ITAE}}(e) = \int_0^t \tau \cdot e(\tau) d\tau \tag{71}$$

where $e(\tau)$ presents the GAEs at time τ, which includes the GAE of relative distance regulation, the GAE of relative course tracking, the GAE of phase separation and the GAE of composition velocity estimation. It can be observed from Equation (71) that, smaller $J_{\mathrm{ITAE}}(e)$ implies smaller convergence error $e(\tau)$ and faster convergence rate.

Due to the process noise in the target motion and the measurement noise in the sensor, the results of a single simulation are not sufficient to illustrate that the proposed method is effective. Hence, we run 300 times Monte-Carlo simulations for scenario 2 to further analyze the performances of the two methods using above defined GAEs and ITAEs.

Figure 14 shows the performance of relative distance regulation. Figure 15 shows the performance of relative course tracking. It can be seen that, the proposed "STTA+CVEA" method has smaller GAEs and ITAEs in relative distance regulation and relative course tracking than that in [31]. It implies that, because of demonstrating smaller convergence errors and faster convergence rates, the "STTA+CVEA" method has better performance than that literature [31] in standoff target tracking mission of a single UAV. The reason for the above phenomenon is that, in contrast to literature [31] only uses the radial distance of offset, the "STTA+CVEA" method updates estimation results according to the offset vector contained more feedback information, and thus our proposed method produce better composition velocity estimation to enhance the tracking performance of the UAV.

Figure 16 shows the performance of composition velocity estimation. We can see that, the GAE and ITAE of composition velocity estimation produced by our "STTA+CVEA" method both are smaller than that in the method of literature [31]. In other words, the estimate results generated in our approach can converge to the true values quickly with smaller convergence errors.

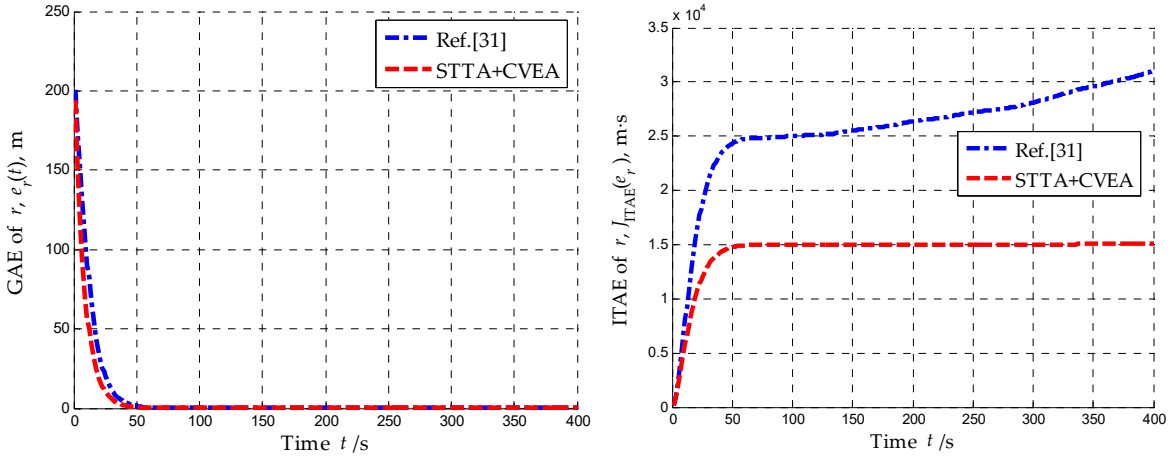

(**a**) GAE, $e_r(t)$ (**b**) ITAE, $J_{\mathrm{ITAE}}(e_r)$

Figure 14. Performance of relative distance regulation (scenario 2). (**a**) Global average error of relative distance. (**b**) Integrated time absolute error of relative distance.

Preprints (www.preprints.org) | NOT PEER-REVIEWED | Posted: 20 July 2023 doi:10.20944/preprints202307.1347.v1

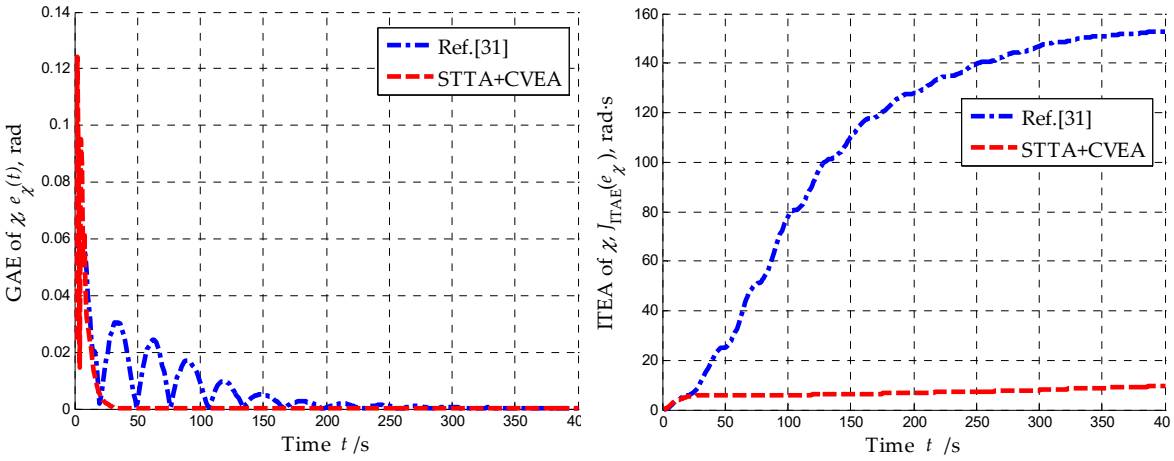

(**a**) GAE, $e_\chi(t)$ (**b**) ITAE, $J_{\mathrm{ITAE}}(e_\chi)$

Figure 15. Performance of relative course tracking (scenario 2). (**a**) Global average error of relative course. (**b**) Integrated time absolute error of relative course.

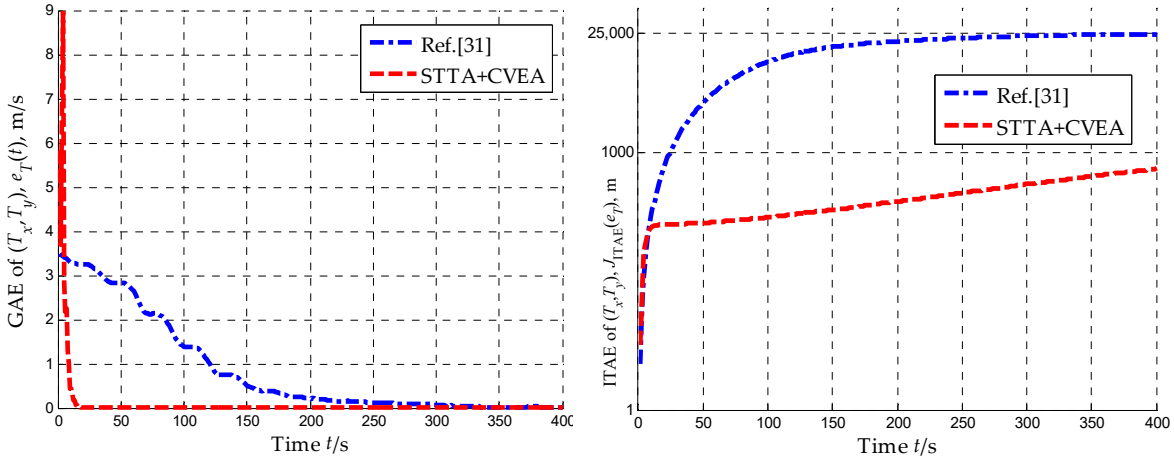

(**a**) GAE, $e_T(t)$ (**b**) ITAE, $J_{\mathrm{ITAE}}(e_T)$

Figure 16. Performance of composition velocity estimation (scenario 2). (**a**) Global average error of composition velocity estimation. (**b**) Integrated time absolute error of composition velocity estimation.

Figure 17 shows the comparison of heading rate control inputs generated by two methods. Figure 18 shows the comparison of relative course errors generated by two methods. In order to show more clearly the curves of u and χ_e, Figures 17 and 18 only plot the histories of u and χ_e in the time period (0-150)s. It can be seen that, due to the CVEA can obtain the composition velocity estimate results accurately and quickly, comparing to the literature [31], the heading rate control input signal is smooth and the relative course error converges to 0 without oscillation. It is confirmed that the CVEA can improve the effectiveness and the robustness of the standoff target tracking algorithm (STTA) for the UAV in unknown background wind.

Preprints (www.preprints.org) | NOT PEER-REVIEWED | Posted: 20 July 2023 doi:10.20944/preprints202307.1347.v1

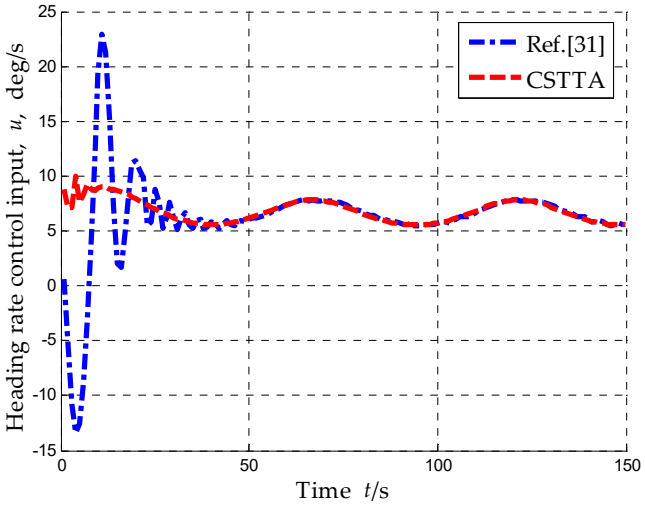

Figure 17. Heading rate control input of UAV, u, (scenario 2).

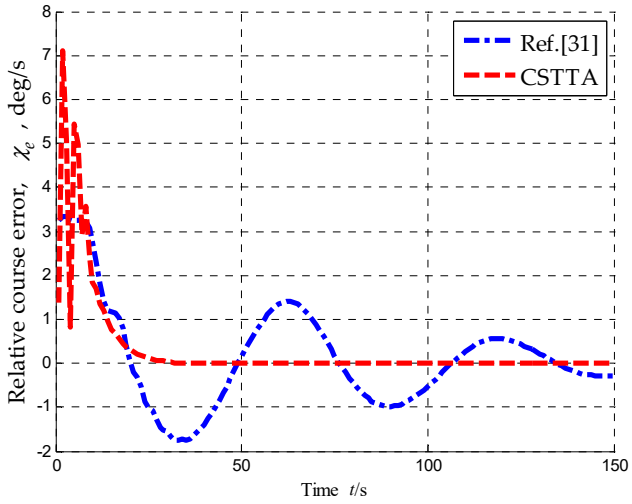

Figure 18. Relative course error of UAV, χ_e, (scenario 2).

The performance comparison of "STTA+CVEA" and literature [31] is shown in Table 1. Comparing to the literature [31], the GAE and ITAE of relative distance regulation are reduced by 29.44% and 43.84% respectively in our proposed method ("STTA+CVEA"). The GAE and ITAE of relative course tracking are reduced by 67.74% and 93.5%, respectively. The GAE and ITAE of composition velocity estimation are reduced by 88.90% and 98.14%, respectively. Therefore, in the standoff target tracking mission using a single UAV in unknown background wind, our method has better performance than literature [31].

Table 1. Performance comparison of "STTA+CVEA" and Ref. [31] (scenario 2).

Control Objective	Performance Index	STTA+CVEA	Ref.[31]	Percentage/(%)
Relative distance regulation	$e_r(t)/\mathrm{m}$	4.2229	5.9846	29.44
	$J_{\mathrm{ITAE}}(e_r)/(m \cdot s)$	1.4436e+004	2.5706e+004	43.84
Relative course tracking	$e_\chi(t)/rad$	0.0020	0.0062	67.74
	$J_{\mathrm{ITAE}}(e_\chi)/(rad \cdot s)$	6.9507	106.9023	93.50
Composition velocity estimation	$e_T(t)/(m \cdot s^{-1})$	0.0954	0.8598	88.90
	$J_{\mathrm{ITAE}}(e_T)/(m)$	313.6534	1.6874e+004	98.14

Preprints (www.preprints.org) | NOT PEER-REVIEWED | Posted: 20 July 2023 doi:10.20944/preprints202307.1347.v1

6.3. Scenario 3: Tracking a Moving Target Using Three UAVs

In scenario 3, three UAVs are used to execute standoff target tracking mission. **Error! Reference source not found.** list the initial settings of A_1, A_2, and A_3, and other simulation conditions are same to scenario 1. In order to verify that the proposed TPSA approach has smaller separation errors and faster convergence rate, and then improves the cooperative tracking performance of the UAVs, the simulation results of the TPSA are compared with the SPSA method in literature [25].

Table 7. The initial settings of UAVs (scenario 3).

UAV A_i	Position(x_i, y_i)/m	Velocity v_i/(m/s)	Heading ψ_i/(deg)
A_1	(600, 200)	100	90
A_2	(-600, 300)	100	120
A_3	(0, 800)	100	-170

Error! Reference source not found. shows the performance of intervehicle phase separation in the process of cooperative standoff target tracking mission using three UAVs. Due to the discontinuity of the wrapped space separation angle led to the oscillation of control input signal, the curve of $e_\theta(t)$ in SPSA method shown in **Error! Reference source not found.**a fluctuates in the convergence process. The fluctuation results in a slow convergence rate which is confirmed by the curve of $J_{\mathrm{ITAE}}(e_\theta)$ in SPSA method shown in **Error! Reference source not found.**b. In contrast to the SPSA method, the curve of $e_\theta(t)$ in our proposed TPSA approach smoothly converges to 0. In summary, comparing to the SPSA method in literature [25], our proposed TPSA has smaller phase separation error and faster convergence rate. The comparison results in others performance indexes are shown in **Error! Reference source not found.**. Comparing to the literature [25], the GAE and ITAE of intervehicle phase separation are reduced by 22.51% and 4.85% respectively in our proposed TPSA method. From **Error! Reference source not found.**, it is verified that, in the cooperative standoff target tracking mission using multiple UAVs in unknown background wind, our proposed CSTTA method has better performance than literature [25].

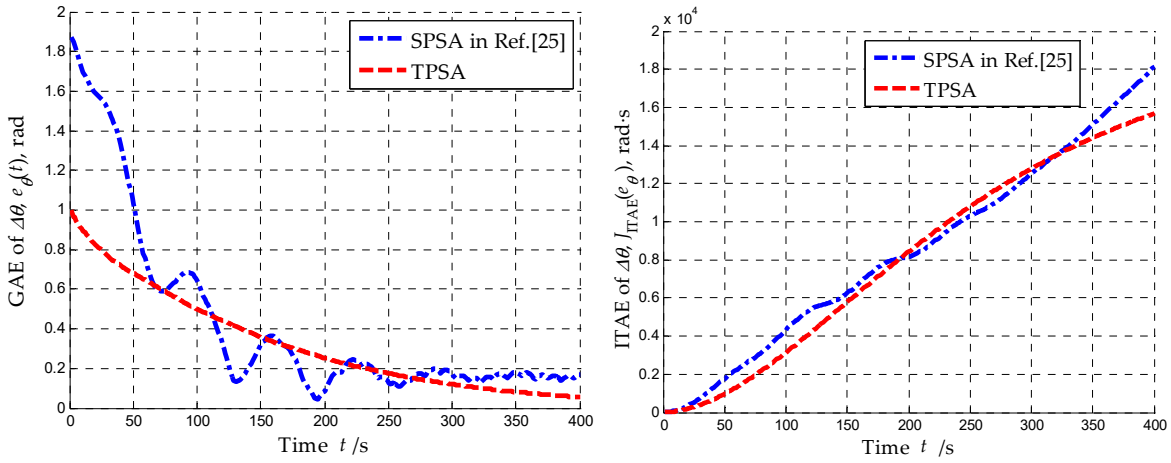

(**a**) GAE, $e_\theta(t)$ (**b**) ITAE, $J_{\mathrm{ITAE}}(e_\theta)$

Figure 19. Performance of intervehicle phase separation (scenario 3). (**a**) Global average error of phase separation. (**b**) Integrated time absolute error of phase separation.

Table 8. Performance comparison of CSTTA and Ref. [25] (scenario 3).

Control Objective	Performance Index	CSTTA	Ref. [25]	Percentage/(%)
Relative distance regulation	$e_r(t)$/m	6.5996	10.7001	38.32
	$J_{\mathrm{ITAE}}(e_r)/(m \cdot s)$	2.5579e+004	5.7246e+004	55.32
Relative course tracking	$e_\chi(t)/rad$	0.0090	0.0135	33.33

Preprints (www.preprints.org) | NOT PEER-REVIEWED | Posted: 20 July 2023 doi:10.20944/preprints202307.1347.v1

	$J_{\mathrm{ITAE}}(e_\chi)/(rad \cdot s)$	21.3996	117.3008	81.76
Intervehicle phase separation	$e_\theta(t)/(rad)$	0.3311	0.4273	22.51
	$J_{\mathrm{ITAE}}(e_\theta)/(rad \cdot s)$	8.0284e+003	8.4378e+003	4.85
Composition velocity estimation	$e_T(t)/(m \cdot s^{-1})$	0.0190	0.5658	96.64
	$J_{\mathrm{ITAE}}(e_T)/(m)$	173.0739	2.4136e+004	99.28

7. Conclusions

This paper investigates the standoff tracking of a ground moving target using multiple fixed-wing UAVs in unknown background wind. The main contribution of this paper is to develop a cooperative standoff target tracking algorithm (CSTTA), which considers the control input constraints of the fixed-wing UAV, target motion, and unknown wind. Following conclusions can be obtained.

(i)A fundamental cooperative standoff target tracking problem include three control objectives: relative distance regulation, relative course convergence and intervehicle phase separation. In addition, in the case of unknown background wind, it is essential to enhance the wind resistance capacity of the UAV.

(ii)A heading rate control law based on LGVF is introduced to regulate the position of a UAV on a circle around the target with a constant standoff distance. It is proved that the proposed heading rate controller can achieve standoff target tracking for a single UAV in the condition of arbitrary initial position and heading. Due to the heading rate input is constrained, the predefined standoff distance between UAV and target has allowable lower bound. The minimum allowable standoff distance is formulated in this paper.

(iii)A new temporal phase separation algorithm (TPSA) is proposed to achieve desired temporal phase separation in cooperative standoff target tracking mission. The TPSA approach takes into account the min and max airspeed constraint, and can avoid the discontinuity of wrapped space phase angle. The results of comparison simulations show that, the TPSA has smaller convergence error and faster convergence rate than the previous space phase separation method.

(iv)The offset between the actual vehicle trajectory and the desired LGVF orbit can be utilized to estimate the composition velocity of target motion and background wind. The results of comparison simulations show that, the proposed composition velocity estimation algorithm (CVEA) can effectively estimate the composition velocity, and thus enhance the tracking performance of the UAVs in the presence of background wind and target motion.

There are many potential directions for future consideration. First, the current models and algorithms will be extended to the three-dimensional coordinates. Second, the proposed algorithms will be implemented on real UAVs in the future works. Third, the more complex mission environment will be considered, and the methods of terrain obstacle and intervehicle collision avoidance will be introduced to enhance aircraft safety. Finally, the communication constraints, such as limited communication range and communication delays, will be considered.

Author Contributions: Conceptualization, Zhong Liu; Data curation, Zhong Liu and Lingshuang Xiang; Formal analysis, Lingshuang Xiang; Funding acquisition, Zemin Zhu; Investigation, Zhong Liu; Methodology, Zhong Liu; Project administration, Zemin Zhu; Resources, Lingshuang Xiang; Software, Zhong Liu; Supervision, Zemin Zhu; Validation, Lingshuang Xiang; Visualization, Zhong Liu; Writing – original draft, Zhong Liu; Writing – review & editing, Lingshuang Xiang.

Funding: This work received fundings from Scientific Research Program of Education Department of Hubei Provincial Government under Grant No. D20212902 and Program of National undergraduate innovation and entrepreneurship under Grant No. 202210514008.

Conflicts of Interest: The authors declare no conflict of interest.

Preprints (www.preprints.org) | NOT PEER-REVIEWED | Posted: 20 July 2023 doi:10.20944/preprints202307.1347.v1

Appendix A. Proof of Lemma 1

Proof. Construct the following function

$$F(\psi) = \frac{v_r}{\lambda_u(\psi)} \tag{A1}$$

Substituting the relative speed v_r given by (6) and $\lambda_u(\psi)$ given by (9) into Equation (A1), it yields that

$$F(\psi) = \frac{(v_s^2 + T^2 - 2v_sT\xi)^{\frac{3}{2}}}{v_s^2 - v_sT\xi} \tag{A2}$$

where $T = \sqrt{T_x^2 + T_y^2}$, $\eta = arctan\left(\frac{T_x}{T_y}\right) \in [-\pi, \pi]$ and $\xi = sin(\psi + \eta) \in [-1, 1]$. Differentiating Equation (A2) with respect to ξ, one has

$$F_\xi(\psi) = \frac{v_sT(v_s^2 + T^2 - 2v_sT\xi)^{\frac{1}{2}}(T^2 + v_sT\xi - 2v_s^2)}{(v_s^2 - v_sT\xi)^2} \tag{A3}$$

When $\xi \in [-1, 1]$, then $F_\xi(\psi) < 0$. It means that, $F(\psi)$ decreases monotonically with increasing ξ. Therefore, when $\xi = -1$, $F(\psi)$ reaches the maximum, i.e., $F(\psi) \le \frac{(v_s+T)^2}{v_s}$. Thus, the proof for Lemma 1 is completed. □

Appendix B. Proof of Lemma 2

Proof. Firstly, two cases are discussed in the proof of the conclusion ①.

(a) When $\chi_e = 0$, then for all $k_1 > 0$, $\dot{\chi}_d = \frac{4v_r r_d^3}{(r^2+r_d^2)^2} \ge -\lambda_u(\psi)\omega_{max} + k_1 sin\chi_e$ is always true.

(b) If $\chi_e \in (0, \pi)$, then we construct the following function

$$F(\chi_e, r) = \frac{1}{sin\chi_e}\left(\dot{\chi}_d + \frac{4v_r}{r_d}\right) \tag{B1}$$

Partial differentiating Equation (B1) with respect to χ_e, one has

$$\frac{\partial F(\chi_e, r)}{\partial \chi_e} = \frac{-4v_r}{r_d sin^2\chi_e}\left[\frac{r_d^4}{(r^2 + r_d^2)^2} + cos\chi_e\right] \tag{B2}$$

It can be observed from Equation (B2) that, when $cos\chi_e^* = -\frac{r_d^4}{(r^2+r_d^2)^2} < 0$, it implies $\chi_e^* \in \left(\frac{\pi}{2}, \pi\right)$, then $F(\chi_e, r)$ reaches the maximum $F(\chi_e^*, r)$, which is express as follows

$$F(\chi_e^*, r) = \frac{v_r}{r}\left(\frac{\zeta}{sin\chi_e^*}\right) + 4\frac{v_r}{r_d}\left(\frac{1}{sin\chi_e^*}\right) \tag{B3}$$

where

$$\zeta = sin\phi_{GF}(1 + cos\phi_{GF})cos\chi_e^* + (cos\phi_{GF} - sin^2\phi_{GF})sin\chi_e^* \tag{B4}$$

For the first term in Equation (B3), one can deduce

$$\frac{\zeta}{sin\chi_e^*} \ge \frac{r_d^4 - r^4 - 4r^2r_d^2}{(r^2 + r_d^2)^2} \tag{B5}$$

For the second term in Equation (B3), one can deduce

$$\begin{aligned}\left(\frac{4v_r}{r_d}\right)\left(\frac{1}{sin\chi_e^*}\right) \ge \left(\frac{4v_r}{r_d}\right)sin\chi_e^* \ge \left(\frac{4v_r}{r_d}\right)\left(\frac{[(r^2 + r_d^2)^2 - r_d^4]^2}{(r^2 + r_d^2)^4}\right)^{\frac{1}{2}} \\ = \left(\frac{4v_r}{r_d}\right)\left(\frac{r^4 + 2r^2r_d^2}{(r^2 + r_d^2)^2}\right)\end{aligned} \tag{B6}$$

According to Equation (B3), one derives

Preprints (www.preprints.org) | NOT PEER-REVIEWED | Posted: 20 July 2023 doi:10.20944/preprints202307.1347.v1

$$\begin{aligned} F(\chi_e, r) \geq F(\chi_e^*, r) &\geq \frac{v_r}{r}\lambda_2 + \left(\frac{4v_r}{r_d}\right) sin\chi_e^* \\ &\geq \frac{v_r}{r}\left(\frac{r_d^4 - r^4 - 4r^2 r_d^2}{(r^2 + r_d^2)^2}\right) + \left(\frac{4v_r}{r_d}\right)\left(\frac{r^4 + 2r^2 r_d^2}{(r^2 + r_d^2)^2}\right) \\ &\xrightarrow{\varepsilon = \frac{r}{r_d}} \frac{v_r}{r_d}\left(1 + \frac{1 - \varepsilon - 4\varepsilon^2 + 6\varepsilon^3 - \varepsilon^4 + 3\varepsilon^5}{\varepsilon(\varepsilon^2 + 1)^2}\right) \\ &> \frac{v_r}{r_d} \end{aligned} \tag{B7}$$

Therefore, let $k_1 = \frac{v_r}{r_d}$, we get $F(\chi_e, r) \geq k_1$, and thus

$$\frac{1}{sin\chi_e}\left(\dot{\chi}_d + \frac{4v_r}{r_d}\right) \geq k_1 \Rightarrow \dot{\chi}_d + \frac{4v_r}{r_d} \geq k_1 sin\chi_e \tag{B8}$$

According to the conclusion of Lemma 1 and Equation (26), it can be obtained that

$$\lambda_u(\psi)\omega_{max} \geq \frac{4v_r}{r_d} \tag{B9}$$

Substituting Equation (B9) into Equation (B8), it yields that

$$\begin{aligned} \dot{\chi}_d + \lambda_u(\psi)\omega_{max} \geq \dot{\chi}_d + \frac{4v_r}{r_d} \geq k_1 sin\chi_e \Rightarrow \dot{\chi}_d \\ \geq -\lambda_u(\psi)\omega_{max} + k_1 sin\chi_e \end{aligned} \tag{B10}$$

The proof of the conclusion ① in Lemma 2 is completed.

Secondly, we prove the conclusion ② of Lemma 2 base on the conclusion ①. To render the proof process simpler, the following function is introduced

$$G(\chi_e) = \begin{cases} \dot{\chi}_d - \lambda_u(\psi)\omega_{max} - k_1 sin\chi_e, \chi_e \in [-\pi, 0) \\ \dot{\chi}_d + \lambda_u(\psi)\omega_{max} - k_1 sin\chi_e, \chi_e \in [0, \pi) \end{cases} \tag{B11}$$

The function $G(\chi_e)$ has this property: if $\chi_e \in [-\pi, 0)$, then $G(\chi_e) = -G(\chi_e + \pi)$. Thus, the conclusion ① of Lemma 2 can be summarized that, $G(\chi_e) = \dot{\chi}_d + \lambda_u(\psi)\omega_{max} - k_1 sin\chi_e \geq 0$ when $\chi_e \in [0, \pi)$. Therefore, when $\chi_e \in [-\pi, 0)$, it implies $\chi_e + \pi \in [0, \pi)$, and then $G(\chi_e) = \dot{\chi}_d - \lambda_u(\psi)\omega_{max} - k_1 sin\chi_e = -G(\chi_e + \pi) \leq 0$. That means the conclusion ② of Lemma 2 is true. Thus, the proof for Lemma 2 is completed. □

Appendix C. Proof of Lemma 3

Proof. The proposed heading rate control law given by (24) can be rewired as follows

$$\begin{aligned} \dot{\chi} = \begin{cases} \Omega, |\Omega| \leq \lambda_u(\psi)\omega_{max} \\ sgn(\Omega)\lambda_u(\psi)\omega_{max}, |\Omega| \geq \lambda_u(\psi)\omega_{max} \end{cases} ; \Omega \\ = -k\lambda_u(\psi)\chi_e + \dot{\chi}_d \end{aligned} \tag{C1}$$

Next, we prove Lemma 3 based on Lemma 2. The following trigonometric inequalities are used in the proof.

$$\begin{cases} \chi_e \geq sin\chi_e, \chi_e \in [0, \pi) \\ \chi_e \leq sin\chi_e, \chi_e \in [-\pi, 0) \end{cases} \tag{C2}$$

(a) When $\chi_e \in [-\pi, 0)$, there are three cases.

- If $\Omega > \lambda_u(\psi)\omega_{max}$, then $\dot{\chi}_e = \lambda_u(\psi)\omega_{max} - \dot{\chi}_d \geq -k_1 sin\chi_e \geq -k_2 sin\chi_e > 0$;
- else if $\Omega < -\lambda_u(\psi)\omega_{max}$, then $\dot{\chi}_e = -\lambda_u(\psi)\omega_{max} - \dot{\chi}_d \geq -k\lambda_u(\psi)\chi_e \geq -k_2\chi_e \geq -k_2 sin\chi_e > 0$;
- else $|\Omega| \leq \lambda_u(\psi)\omega_{max}$, then $\dot{\chi}_e = -k\lambda_u(\psi)\chi_e \geq -k_2\chi_e \geq -k_2 sin\chi_e > 0$.

In summary, when $\chi_e \in [-\pi, 0)$, $\dot{\chi}_e \geq -k_2 sin\chi_e > 0$. It means the conclusion ① of Lemma 3 is true.

(b) When $\chi_e \in [0, \pi)$, there are three cases.

- If $\Omega > \lambda_u(\psi)\omega_{max}$, then $\dot{\chi}_e = \lambda_u(\psi)\omega_{max} - \dot{\chi}_d \leq -k\lambda_u(\psi)\chi_e \leq -k_2 sin\chi_e < 0$;

Preprints (www.preprints.org) | NOT PEER-REVIEWED | Posted: 20 July 2023 doi:10.20944/preprints202307.1347.v1

- else if $\Omega < -\lambda_u(\psi)\omega_{max}$, then $\dot{\chi}_e = -\lambda_u(\psi)\omega_{max} - \dot{\chi}_d \le -k_1 sin\chi_e \le -k_2 sin\chi_e < 0$;
- else $|\Omega| \le \lambda_u(\psi)\omega_{max}$, $\dot{\chi}_e = -k\lambda_u(\psi)\chi_e \le -k_2 sin\chi_e < 0$.

In summary, when $\chi_e \in [0, \pi)$, $\dot{\chi}_e \le -k_2 sin\chi_e < 0$. It means the conclusion ② of Lemma 3 is true. Thus, the proof for Lemma 3 is completed. □

Appendix D. Proof of Lemma 4

Proof. according to (9), we can obtain $\dot{r} = v_r cos(\chi - \theta) = v_r cos(\phi_{GF} + \chi_e) \le v_r$. It can be observed from (6) that, $v_r \le v_s + T$, it implies $\dot{r} \le v_r \le v_s + T$. Thus, it can be concluded that

$$r \le r_0 + (v_s + T)t_c \tag{D1}$$

where r_0 presents the initial relative distance between the UAV and the target at time t_0. t_c presents the time of the relative course error χ_e converging to 0.

(a) If $|\chi_{e0}| \in \left[0, \frac{\pi}{2}\right]$, it can be obtained that, the converge time t_{c1} of process $(\chi_e \to 0)$.

$$t_{c1} = \frac{1}{k_2} \ln \left| \frac{\tan\left(\frac{\chi_{e0}}{2}\right)}{\tan\left(\frac{\alpha_0}{2} - \frac{\pi}{4}\right)} \right| \tag{D2}$$

Substituting (D2) into (D1), the upper bound of r is obtained as follows

$$r \le r_0 + (v_s + T)\frac{1}{k_2} ln \left| \frac{tan\left(\frac{\chi_{e0}}{2}\right)}{tan\left(\frac{\alpha_0}{2} - \frac{\pi}{4}\right)} \right| \tag{D3}$$

(b) If $|\chi_{e0}| \in \left(\frac{\pi}{2}, \pi\right]$, the relative course error $|\chi_e|$ firstly converges to π/2 in time t_{c2}, and then converges from π/2 to 0 in time t_{c3}. According to Equation (32), one has

$$t_{c2} = \frac{1}{k_2} ln \left| tan\left(\frac{\chi_{e0}}{2}\right) \right| \tag{D4}$$

$$t_{c3} = \frac{1}{k_2} ln \left| \frac{1}{tan\left(\frac{\alpha_0}{2} - \frac{\pi}{4}\right)} \right| \tag{D5}$$

Thus, the upper bound of r is defined

$$\begin{aligned} r &\le r_0 + (v_s + T) \cdot (t_{c2} + t_{c3}) \\ &= r_0 + (v_s + T)\frac{1}{k_2} ln \left| \frac{tan\left(\frac{\chi_{e0}}{2}\right)}{tan\left(\frac{\alpha_0}{2} - \frac{\pi}{4}\right)} \right| \end{aligned} \tag{D6}$$

In summary, the relative distance r between the drone and the target is bounded, so lemma 4 is proved. □

References

1. Guo, B.; Vu, D.; Xu, L.; Xue, M.; Li, J. Ground moving target indication via multichannel airborne SAR[J]. IEEE Transactions on Geoscience & Remote Sensing, **2011**, 49(10):3753-3764.
2. Zhong, L.; Xiaowei, F.; Xiaoguang. G. Co-Optimization of communication and sensing for multiple unmanned aerial vehicles in cooperative target tracking [J]. Applied Sciences, **2018**, 8(6), 899.
3. Li, Z.; Chen, X .; Zhao, Z. Design of standoff cooperative target-tracking guidance laws for autonomous unmanned aerial vehicles[J]. Mathematical Problems in Engineering, **2021**, 2021(2):1-14.
4. Zhoufan, X.; Ruixuan W.; Xiaolin Z.; Shulei W. Coordinated standoff target tracking guidance method for UAVs[J]. IEEE Access, **2018**, 6(11): 59853-59859.
5. Hyondong, O.; Seungkeun, K.; Hyo-sang, S.; Antonios, T. Coordinated standoff tracking of moving target groups using multiple UAVs [J]. IEEE Transactions on Aerospace & Electronic Systems, **2015**, 51(2): 1501-1514.
6. Rysdyk, R.; Lum, C.; Vagners, J. Autonomous orbit coordination for two unmanned aerial vehicles [C]. // In Proceeding of the AIAA Guidance, Navigation, and Control Conference and Exhibit, San Francisco, CA, USA, 15–18 August **2005**.

7. Ducard, G.; Kulling, K. C.; Geering, H. P. A simple and adaptive on-line path planning system for a UAV[C]. //Proceedings of the 15th Mediterranean Conference on Control and Automation, Piscataway, IEEE, **2007**: 1-6.
8. Park, S.; Deyst, J.; How J. P. Performance and Lyapunov stability of a nonlinear path-following guidance method [J]. Journal of Guidance, Control, and Dynamics, **2007**, 30(6): 1718 - 1728.
9. Park, S. Guidance law for standoff tracking of a moving object [J]. Journal of Guidance, Control, and Dynamics, **2017**, 40(11):2948–2455.
10. Frew, E. W.; Lawrence, D. A.; Steve, M. Coordinated standoff tracking of moving targets using Lyapunov guidance vector fields [J]. Journal of Guidance Control & Dynamics, **2008**, 31(2):290-306.
11. Chen, H.; Chang, K.; Agate, C. S. UAV Path Planning with tangent-plus-Lyapunov vector field guidance and obstacle avoidance [J]. IEEE Transactions on Aerospace and Electronic Systems, **2013**, 49(2): 840 - 856.
12. Pothen, A. A.; Ratnoo, A. Curvature-constrained Lyapunov vector field for standoff target tracking [J]. Journal of Guidance, Control, and Dynamics, **2017**, 40(10): 2729–2736.
13. Lim, S.; Kim, Y.; Lee, D.; Bang, H. Standoff target tracking using a vector field for multiple unmanned aircrafts[J]. Journal of Intelligent & Robotic Systems, **2013**, 69(1-4):347-360.
14. Sun, S.; Wang, H.; Liu, J.; He, Y. Fast Lyapunov vector field guidance for standoff target tracking based on offline search[J]. IEEE Access, **2019**, 7: 124797 - 124808.
15. Bishopa, A.N.; Fidanb, B.; Andersonb, B.D.O.; Do ˘gançayc, K.; Pathirana, P.N. Optimality analysis of sensor-target localization geometries. Automatica **2010**, 46, 479–492.
16. Kim, S.; Oh, H.; Tsourdos. A. Nonlinear model predictive coordinated standoff tracking of a moving ground vehicle [J]. Journal of Guidance, Control, and Dynamics, **2013**, 36(2):557-566.
17. Sun, S.; Liu, Y.; Guo, S.; Gang, L. Observation-driven multiple UAV coordinated standoff target tracking based on model predictive control [J]. Tsinghua Science & Technology, **2022**, 27(6):948-963.
18. Zhang, M., T. Liu, H.H. Cooperative Tracking a Moving Target Using Multiple Fixed-wing UAVs [J]. Journal of Intelligent & Robotic Systems, **2015**, 81: 505-529.
19. He, S.; Wang, J.; Lin, D. Unknown ground moving target tracking using multiple unmanned aerial vehicles [J]. Proceedings of the Institution of Mechanical Engineers, Part G: Journal of Aerospace Engineering, **2019**, 233(3): 1021 - 1032.
20. Yoon, S.; Park, S.; Kim, Y. Circular motion guidance law for coordinated standoff tracking of a moving target [J]. IEEE Transactions on Aerospace and Electronic Systems, **2013**, 49(4): 2440–2462.
21. Yao, P.; Wang, H. L.; Su, Z. K. Cooperative path planning with applications to target tracking and obstacle avoidance for multi-UAVs[J].Aerospace Science & Technology, **2016**, 54:10-22.
22. Kokolakis, N. M. T.; Koussoulas, N. T. Coordinated standoff tracking of a ground moving target and the phase separation problem [C]. // 2018 International Conference on Unmanned Aircraft Systems (ICUAS), Dallas, IEEE, **2018**, pp. 473–482.
23. Song, Z.; Li, H.; Chen, C.; Zhou, X.; Xu F. Coordinated standoff tracking of moving targets using differential geometry [J]. Journal of Zhejiang University SCIENCE C, **2014**, 15(4): 284-292.
24. Che, F.; Niu, Y.; Li, J.; Wu, L. Cooperative standoff tracking of moving targets using modified Lyapunov vector field guidance [J]. Applied Sciences, **2020**, 10(11): 3709.
25. Kokolakis, N. M. T.; Koussoulas, N. T. Robust standoff target tracking with finite-time phase separation under unknown wind [J].Journal of Guidance Control and Dynamics, **2021**, 44(2): 1183-1198.
26. Harinarayana, T.; Hota, S.; Kushwaha, R. Vector field guidance for standoff target tracking [J]. Proceedings of the Institution of Mechanical Engineers, Part G: Journal of Aerospace Engineering, **2022**, 236(14): 2963 - 2973.
27. Rysdyk, R. Unmanned aerial vehicle path following for target observation in wind [J]. Journal of Guidance, Control, and Dynamics, **2006**, 29(5): 1092 – 1100.
28. Sun, S.; Dong, K.; Guo, C.; Tan, D. A wind estimation based on unscented kalman filter for standoff target tracking using a fixed-wing UAV [J]. International Journal of Aeronautical and Space Sciences, **2020**(22): 366-375.
29. Beal, T. R. Digital simulation of atmospheric turbulence for Dryden and von Karman models." Journal of Guidance, Control, and Dynamics, **1993**, 16(1): 132–38.
30. Gawronski, W. Modeling wind-gust disturbances for the analysis of antenna pointing accuracy [J]. IEEE Antennas and Propagation Magazine, **2004**, 46(1): 50- 58.
31. Summers, T. H.; Akella, M. R.; Mears, M. J. Coordinated standoff tracking of moving targets: control laws and information architectures [J]. Journal of Guidance, Control, and Dynamics, **2006**, 32(1):56–69.